JGR Oceans

RESEARCH ARTICLE
10.1029/2019JC015052

Key Points:
- The surface sampling scheme of the Drake Passage Time-series program robustly captures mixed-layer biogeochemistry
- Surface silicate and nitrate vary distinctly by frontal zone and season, each driven by unique physical and biological processes
- Observational constraints on the seasonal cycling of nutrients serve as a metric for validating and improving biogeochemical models

Supporting Information:
- Supporting Information S1

Correspondence to:
N. M. Freeman,
n2freeman@ucsd.edu

Citation:
Freeman, N. M., Munro, D. R., Sprintall, J., Mazloff, M. R., Purkey, S. G., Rosso, I., et al. (2019). The observed seasonal cycle of macronutrients in Drake Passage: Relationship to fronts and utility as a model metric. *Journal of Geophysical Research: Oceans*, *124*, 4763–4783. https://doi.org/10.1029/2019JC015052

Received 20 FEB 2019
Accepted 20 MAY 2019
Accepted article online 24 MAY 2019
Published online 10 JUL 2019

The Observed Seasonal Cycle of Macronutrients in Drake Passage: Relationship to Fronts and Utility as a Model Metric

Natalie M. Freeman[1], David R. Munro[2,3], Janet Sprintall[1], Matthew R. Mazloff[1], Sarah Purkey[1], Isabella Rosso[1], Carissa A. DeRanek[1,4], and Colm Sweeney[3]

[1]Scripps Institution of Oceanography, University of California, San Diego, La Jolla, CA, USA, [2]Cooperative Institute for Research in Environmental Sciences, University of Colorado Boulder, Boulder, CO, USA, [3]NOAA Earth System Research Laboratory, Boulder, CO, USA, [4]Department of Biology, Harvey Mudd College, Claremont, CA, USA

Abstract The Drake Passage Time-series (DPT) is used to quantify the spatial and seasonal variability of historically undersampled, biogeochemically relevant properties across the Drake Passage. From 2004–2017, discrete ship-based observations of surface macronutrients (silicate, nitrate, and phosphate), temperature, and salinity have been collected 5–8 times per year as part of the DPT program. Using the DPT and Antarctic Circumpolar Current (ACC) front locations derived from concurrent expendable bathythermograph data, the distinct physical and biogeochemical characteristics of ACC frontal zones are characterized. Biogeochemical-Argo floats in the region confirm that the near-surface sampling scheme of the DPT robustly captures mixed-layer biogeochemistry. While macronutrient concentrations consistently increase toward the Antarctic continent, their meridional distribution, variability, and biogeochemical gradients are unique across physical ACC fronts, suggesting a combination of physical and biological processes controlling nutrient availability and nutrient front location. The Polar Front is associated with the northern expression of the Silicate Front, marking the biogeographically relevant location between silicate-poor and silicate-rich waters. South of the northern Silicate Front, the silicate-to-nitrate ratio increases, with the sharpest gradient in silicate associated with the Southern ACC Front (i.e., the southern expression of the Silicate Front). Nutrient cycling is an important control on variability in the surface ocean partial pressure of carbon dioxide (pCO_2). The robust characterization of the spatiotemporal variability of nutrients presented here highlights the utility of biogeochemical time series for diagnosing and potentially reducing biases in modeling Southern Ocean pCO_2 variability, and by inference, air-sea CO_2 flux.

Plain Language Summary Nutrients fuel phytoplankton communities that are important in the marine food web and global carbon cycling. Understanding modern-day nutrient availability and its physical and biological drivers is critical to accurately predict future climate with models. The Southern Ocean helps regulate climate and is vulnerable to future change, but as one of the least sampled oceans, physical and biogeochemical processes are still not fully understood. This study uses the 13-year Drake Passage Time-series, the longest year-round biogeochemical time series in the Southern Ocean, to quantify nutrient availability and variability on seasonal time scales. Across Drake Passage, temperatures decrease and nutrients increase toward Antarctica, exhibiting sharp gradients at currents and creating conditions favoring distinct phytoplankton groups. Nutrients are used by phytoplankton in summer and regenerated and resupplied by mixing in winter; these processes draw surface ocean carbon down in summer and increase carbon in winter. While nitrate is a necessary nutrient for all phytoplankton, silicate is only required by a single major phytoplankton group. Simultaneous observations of both nutrients allows us to better understand group-specific productivity and, ultimately, its impact on climate.

1. Introduction

As human-sourced atmospheric carbon dioxide (CO_2) concentrations continue to rise, quantifying the sources and sinks of CO_2 and improving our mechanistic understanding of global carbon cycling is critical. This is particularly important in the Southern Ocean which accounts for more than 40% of the total ocean anthropogenic CO_2 sink and ~75% of the oceanic uptake of anthropogenic heat (Frölicher et al., 2014). Since the mid-twentieth century, this vast polar ocean has been rapidly warming and freshening, driven by increas-

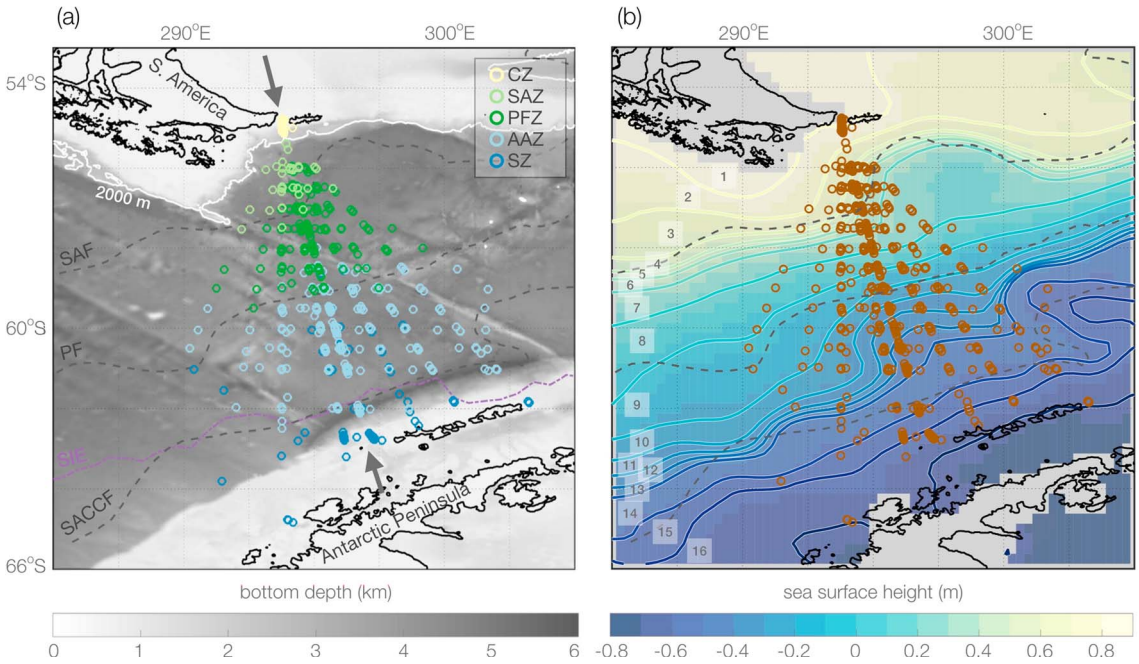

Figure 1. Discrete sampling locations (open circles) of the Drake Passage Time-series (DPT) program from 2004–2017; ~57% of sampling occurred along a common transect line, indicated by arrows in (a). The Orsi et al. (1995) front positions (dark gray dashed contours) are indicated in (a) and (b): the Subantarctic Front (SAF), Polar Front (PF), and Southern ACC Front (SACCF). In (a), DPT sampling locations are colored by expendable bathythermograph-defined frontal zone at the time of crossing overlain on bathymetry (grayscale map; ETOPO1; Amante & Eakins, 2009): Subantarctic Zone (SAZ; pale green), Polar Frontal Zone (PFZ; green), Antarctic Zone (AAZ; pale blue), and Southern Zone (SZ; blue); the Coastal Zone (CZ) is indicated in yellow and delineated by the local 2,000-m isobath (white contour). In (a), the 2004–2017 September mean sea ice extent (SIE) is indicated (purple dashed contour; Remote Sensing Systems, 2016). In (b), DPT sampling locations (brown open circles) are overlain on the 2004–2017 mean standardized sea surface height (SSH; color map) from Archiving, Validation and Interpretation of Satellite Oceanographic; SSH zones are numbered and demarcated by lines of constant SSH (color contours), marking the local bin bounds used in the analysis (see section 2.1.1; see Table S1).

ing greenhouse gases and depletion of ozone (Swart et al., 2018). Such large-scale changes have implications for physical and biogeochemical processes at the local and basin scale, including biological productivity and the air-sea flux of heat and carbon.

As the southern link of the global overturning circulation, the Southern Ocean plays a critical role in regulating climate through carbon and heat exchange (Rintoul et al., 2001). Here a surface-to-deep ocean connection exists through upwelling pathways along strongly tilted isopycnals allowing for deep water mass ventilation, transformation at the surface, and subduction of newly formed water masses (Rintoul, 2018). Furthermore, the land opening of Drake Passage allows for interbasin exchange of water masses via the zonally unbounded, eastward-flowing Antarctic Circumpolar Current (ACC). Physical and biological processes and regional bathymetry in the Southern Ocean drive deep-reaching, persistent physical and chemical fronts (Freeman et al., 2018; Palter et al., 2013; Sprintall, 2003) that divide the region into distinct physical and biogeochemical zones (i.e., delineate water mass boundaries; Pollard et al., 2002). From north to south, the historically defined physical ACC fronts and frontal zones are the Subantarctic Zone (SAZ), Subantarctic Front (SAF), Polar Frontal Zone (PFZ), Antarctic Polar Front (PF), Antarctic Zone (AAZ), Southern ACC Front (SACCF), and Southern Zone (SZ; which also includes the region sometimes referred to as the Seasonal Ice Zone; Figure 1; Baker et al., 1977). Wind-driven upwelling ventilates Circumpolar Deep Water (CDW) rich in nutrients and carbon south of the PF (Toggweiler & Samuels, 1995). These transformed waters feed mode and intermediate waters that move northward under the subtropical gyres (e.g., Subantarctic Mode Water and Antarctic Intermediate Water; Deacon, 1933, 1937). These upwelling processes control nutrient supply and impact phytoplankton communities throughout the global oceans that are critical for marine food web dynamics and the efficiency of the biological pump (Matsumoto et al., 2002; Moore et al., 2018; Sarmiento et al., 2004).

The resulting property distributions and gradients at physical ACC fronts imprint on the biogeography of Drake Passage, with diatoms largely dominating the silicate-rich waters south of the Silicate Front (SF; the

sharp silicate gradient at the PF) and coccolithophores and other small phytoplankton groups more abundant north of the SF (Balch et al., 2016; Nissen et al., 2018; Trull et al., 2018). The ratio of calcifiers and silicifiers has implications for global phytoplankton biomass, annual net primary production, organic carbon export as ballast, and air-sea CO_2 exchange through photosynthesis and calcification. Previous studies show that coccolithophores have shifted poleward in recent decades (e.g., Winter et al., 2013) and that the SF is predicted to shift poleward in the future, driven by large-scale reductions in macronutrients (Freeman et al., 2018; Moore et al., 2018). Our ability to predict how phytoplankton communities will respond to future climate change hinges on our understanding of modern-day biogeography and its representation in biogeochemical models. While a better understanding of the spatial structure and temporal variability of the ACC has been the priority of recent observational and modeling studies (e.g., Donohue et al., 2016; Freeman et al., 2016, 2018; Graham et al., 2012; Gille, 2014; Sallée et al., 2008; Sokolov & Rintoul, 2009), the biogeochemistry of the ACC is still poorly understood. The historical lack of repeat year-round coordinated measurements of hydrographic and biogeochemical properties, particularly in austral winter when ship-based sampling conditions are poor, translates to poor representation of these important seasonal processes in current state-of-the-art biogeochemical models.

Our current understanding of the drivers of CO_2 flux in the Southern Ocean is limited to a few observation-based studies which are heavily weighted toward the Drake Passage Time-series (DPT; Gregor et al., 2018; Fay et al., 2018; Landschützer et al., 2015; Munro, Lovenduski, Takahashi, et al., 2015). The variability in the strength of the Southern Ocean carbon sink on seasonal time scales is largely driven by compensatory variations in temperature, biology, and vertical exchange with the enriched deep waters, which in turn, drive variability on interannual time scales (Gregor et al., 2018; Takahashi et al., 1993). The DPT is the only multiyear, year-round ship-based biogeochemical sampling program in the Southern Ocean and, in particular, the ACC. Since 2002, the DPT's coordinated effort to measure both hydrographic and biogeochemical properties has provided sufficient data to resolve the annual cycle of the carbonate system. However, current state-of-the-art biogeochemical models, including those used in the Fifth Coupled Model Intercomparison Project (CMIP5), do not adequately resolve the annual cycle of surface ocean partial pressure of CO_2 (pCO_2) and, thus, CO_2 flux (Gruber et al., 2019; Lenton et al., 2013; Jiang et al., 2014; Mongwe et al., 2016, 2018; Rödenbeck et al., 2015). Many Earth System Models struggle with the temperature-dependent component of pCO_2 variability that is too large, failing to strike the appropriate balance between wintertime mixing and summertime biological processes (Mongwe et al., 2018). While previous studies have used direct comparisons of observed and modeled pCO_2 to diagnose and/or tune model biases (e.g., Jiang et al., 2014; Mongwe et al., 2018), less attention has been paid to robustly resolving the seasonal cycles of nutrients (e.g., nitrate) as a first-order validation. Nutrient variability signifies a portion of the nontemperature-dependent component of pCO_2 variability, as a limiting factor in the biological pump (Munro, Lovenduski, Stephens, et al., 2015). Therefore, the realistic representation of nutrient cycling in models is vital to understanding and robustly modeling pCO_2 flux.

In this study, we utilize the DPT to provide a first estimate of the spatial and seasonal variability of silicate, nitrate, and phosphate concentration, temperature, and salinity across the ACC in Drake Passage from 2004–2017. We examine the observed physical and biogeochemical variability of ACC frontal zones on seasonal time scales, with front locations defined by temperature criterion using high-resolution expendable bathythermograph (XBT) data (section 3.1). We quantify the mean property distributions across Drake Passage and identify the locations of the biogeochemical fronts of silicate and nitrate that are important for supporting local phytoplankton communities and influencing their biogeography (section 3.2). We further employ ship- and float-based measurements to connect the biogeochemical variability observed at the surface with the mixed layer and confirm that the DPT robustly represents the surface mixed layer (section 3.3). Finally, we use output from a data assimilating model to demonstrate the utility of the DPT in diagnosing and potentially reducing model biases in Southern Ocean carbon cycling (section 3.4). We discuss these results and the modeling exercise in section 4.

2. Data and Methods

2.1. The DPT

The repeat DPT program is the longest year-round time series of coordinated in situ sampling across ACC latitudes in the Southern Ocean. Discrete surface (<4 m) samples have been collected on five to eight transects annually across the Drake Passage from the Antarctic Research Supply Vessel Laurence M. Gould's

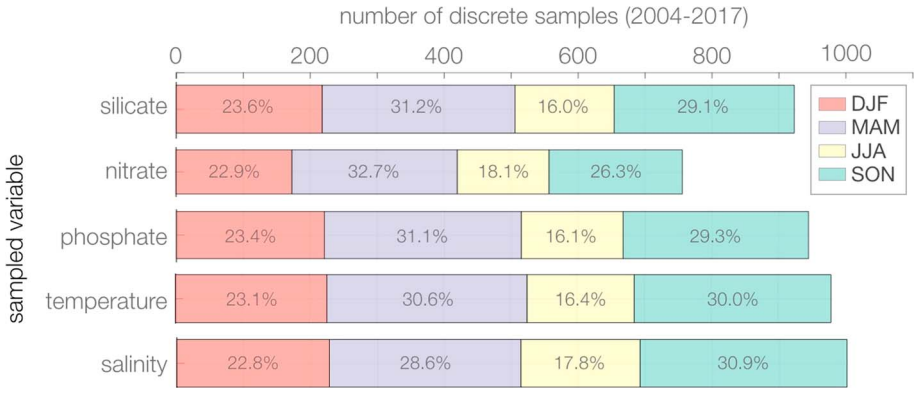

Figure 2. Number of discrete observations of silicate, nitrate, phosphate, temperature, and salinity collected as part of the Drake Passage Time-series program between 2004 and 2017 (after quality control). Bars are colored and labeled (percentage values) to indicate the proportion of samples collected in a given season: December-January-February (DJF; austral summer), March-April-May (MAM; austral autumn), June-July-August (JJA; austral winter), or September-October-November (SON; austral spring).

(LMG) underway system. DPT samples are taken at ~50-km spacing (equating to ~15 locations) across the ~700-km opening of Drake Passage between South America and the Antarctic Peninsula. In this study we analyze DPT measurements of silicate, nitrate, and phosphate concentration and temperature and salinity spanning November 2004 to September 2017 (75 total crossings; Figure 1).

The historical paucity of Southern Ocean observations is most pronounced in wintertime, when poor weather conditions often preclude ship-based collection. However, the DPT is unique, boasting year-round biogeochemical sampling, where austral winter observations make up more than 16% of our 2004–2017 data set (Figure 2). During this time period, austral summer (DJF) and spring (SON) have been sampled every year, autumn (MAM) was not sampled in 2011, and winter (JJA) was not observed in the years 2004, 2007, 2010, and 2012–2013.

Since December 2014, discrete samples for macronutrients have been collected in 30-ml polypropylene bottles, frozen and shipped on dry ice (−80 °C), and analyzed by the Ocean Data Facility at Scripps Institution of Oceanography. Prior to December 2014, samples were analyzed by the Chesapeake Biological Laboratory. Analytical precision based on the mean standard deviation of replicate pairs ($n = 13$) is 0.9, 0.5, and 0.02 mmol/m^3 for silicate, nitrate, and phosphate, respectively. A two-step quality control process is utilized for nutrient observations. First, nitrate outliers are removed based on deviation from expected nutrient ratios. This step accounts for higher variability in nitrate during the period preceding December 2014. Second, through an iterative computation, any DPT samples that fall outside six, then five, and ultimately four standard deviations of the mean data distribution within each frontal zone (see section 2.2) are removed prior to analysis. Any difference in the number of total measurements between sampled variables shown in Figure 2 is the result of this two-step quality control process. Details on DPT pCO_2 measurements are described elsewhere (Munro, Lovenduski, Stephens, et al., 2015; Munro, Lovenduski, Takahashi, et al., 2015).

2.1.1. DPT Data Gridding

While ~58% of the DPT ship crossings fall along a common line between South America and the Antarctic Peninsula (indicated by arrows in Figure 1a), the remaining crossings are spatially heterogeneous, with samples collected in different locations from year to year, particularly in southern Drake Passage. To minimize spatial aliasing, we bin the data onto a common grid in two independent ways: by frontal zone (Figure 1a) and by sea surface height (SSH; Figure 1b). Alternate binning schemes were tested with no significant impacts on the results (not shown).

2.1.2. Frontal Zone Binning Scheme

In order to quantify the mean spatial and seasonal variability of the physical and biogeochemical zones across Drake Passage, we bin each discrete sample by month and XBT-defined frontal zone (section 2.2), resulting in 4 monthly time series from 2004–2017 (color circles in Figure 1a). We define a fifth zone, the Coastal Zone (CZ; yellow circles in Figure 1a), which encompasses DPT samples collected in waters shallower than 2,000 m off the coast of South America (white contour in Figure 1a).

2.1.3. SSH Zone Binning Scheme

To identify the location of nutrient fronts, marked by a sharp meridional gradient in concentration, we bin each discrete sample based on the local reference mean SSH (averaged over months consistent with the DPT, November 2004 to September 2017). This second, independent binning scheme is designed to retain most of the original sampling resolution of each crossing (~50 km) while taking into account the meandering flow of the ACC. We use the 1/4° gridded monthly mean Absolute Dynamic Topography product from AVISO (Archiving, Validation and Interpretation of Satellite Oceanographic), which is derived from multiple altimeters and distributed by the Copernicus Marine and Environment Monitoring Service.

To account for basin-scale mass and heat variability, we first remove the monthly spatial mean (53–66° S, 284–307° E) offset from the monthly SSH time series; the temporal average of this November 2004 to September 2017 standardized SSH time series is shown in Figure 1b. We colocate this average SSH with each discrete sampling location, creating a SSH data set on the DPT grid. To determine the bin bounds of each SSH zone (color contours in Figure 1b and supporting information Table S1), we quantify the mean DPT SSH at equal 0.5° spacing southward across Drake Passage, starting from the northernmost DPT sampling location (54.8° S). Each DPT sample is then binned by SSH, according to these bin bounds. The SSH zones used in this study are shown in Figure 1b, and their detailed specifications are listed in Table S1.

SSH (and the magnitude of its variability) decreases toward the Antarctic continent (Sprintall, 2003), with the southern Drake Passage south of the PF characterized by relatively weak surface flows (i.e., weaker SSH gradients). Therefore, north-south spacing of SSH bins is not linear, with increasingly higher bin spacing resolution found in the southern portion of the DPT sampling grid (Figure 1 and Table S1). When comparing results from our SSH binning scheme to those from previously used methodologies (e.g., the 30° rotation method used in Munro, Lovenduski, Takahashi, et al., 2015), our method has the ability to average along the meridional meanders characteristic of ACC flow and therefore reduces averaging properties across distinct water masses. We also find little difference between using a reference time-averaged SSH (this study) and a time-dependent SSH field (e.g., monthly SSH). Since the SSH bin bounds are found locally, this binning method can be applied to any data set.

2.2. XBT-Defined ACC Fronts

We use temperature data from XBTs to identify the latitude of the three major ACC fronts along each DPT transect. Since 1996, XBTs have been launched from the LMG as part of the Scripps High-resolution XBT Program (HRX line AX22; Sprintall, 2003). To resolve temperature variations across fronts and other mesoscale features of the ACC, these Sippican Deep Blue probes are dropped at ≤15-km spacing and provide the finer-scale temperature structure of the upper ~800 m of Drake Passage. As part of the HRX program, XBT data undergo a quality control process that includes a correction for errors in fall rates by applying the Hanawa et al. (1995) equation.

We use HRX XBT profiles averaged at 10-m vertical resolution to identify ACC front locations using the following definitions (as in Sprintall, 2003):

1. SAF: at 300 m, the maximum temperature gradient found between 3 and 5 °C (after Sievers & Emery, 1978);
2. PF: at 200 m, the northern extent of the 2 °C isotherm (after Joyce et al., 1978; Orsi et al., 1995); and
3. SACCF: between 200 and 500 m, the southernmost extent of the 1.8 °C isotherm along the maximum temperature gradient.

Front latitudes are gridded in time to create a monthly time series over the DPT period. Open-ocean frontal zones are defined as the waters found between persistent physical ACC fronts. The temperature-defined location of the SACCF is not as reliable as a velocity-defined SACCF (Lenn et al., 2007); hence, the SZ south of the SACCF is less well defined than the other ACC frontal zones.

2.3. Repeat Hydrography: SR01

To connect the surface properties observed by the DPT to the upper water column, we show two seasonal snapshots of the upper 500 m across Drake Passage. As part of the DPT project, the LMG was also used for two high-quality, hydrographic occupations of the World Ocean Circulation Experiment (WOCE) SR01 line in March 2006 (WOCE ID 33LG2006; Sweeney et al., 2012) and again in September 2009 (WOCE ID 33LG2009) to characterize differences between austral late summer-early autumn and late winter-early spring. Full-depth vertical profiles of silicate, nitrate, temperature, and salinity were collected at stations spaced at ~30–60 km. We select these two complete SR01 lines, traversing 56–61° S along the most repeated

line of the DPT program (indicated by arrows in Figure 1a). Only SR01 data with good quality (WOCE) flags were included in the analysis. Additionally, data from one duplicate station (at 59.5° S and 63.4° W) occupied during 33LG2006 were removed prior to analysis. Temperature (°C; ITS–90) and salinity (practical salinity [psu]) profiles are used to calculate potential temperature (°C; Bryden, 1973; Fofonoff & Millard, 1983). Data cross sections are constructed by regularly gridding the data in depth (1 dbar in pressure) and latitude (0.1° latitude).

2.4. Biogeochemical Profiling Floats

Additionally, we utilize data from Biogeochemical-Argo (BGC-Argo) floats that have passed through the region to evaluate how well the DPT surface sampling scheme represents the surface mixed layer. The Southern Ocean Carbon and Climate Observations and Modeling project deploy BGC-Argo floats equipped with conductivity-temperature-depth, pH, nitrate, oxygen, and optical sensors throughout the Southern Ocean. The floats vertically profile the upper 2,000 m every 10 days. Between December 2015 and June 2018, seven BGC-Argo floats traversing Drake Passage provided 126 total vertical profiles of nitrate, temperature, and salinity between the surface and 2,000 m; three floats provided 28 profiles north of the Orsi et al. (1995) PF; and four floats provided 98 profiles south of the PF (Figure 3a and Table S2).

Potential temperature (°C) is calculated prior to analysis; salinity is reported on the practical salinity scale. BGC-Argo float vertical profiles are linearly interpolated onto a common vertical grid with 1-m resolution, preserving the fine vertical structure in the upper water column. In this study, we only include floats with profiles within a domain encompassing the DPT sampling grid (opaque colored circles in Figure 3a): 288–304° E and 53–66° S. The mixed layer depth (MLD) of each profile is calculated using a 0.03 kg/m^3 density threshold (de Boyer Montégut et al., 2004). For each profile, we compute Pearson's correlation coefficients (r) for each measured value at depth relative to the average surface value, defined as the vertical mean of the top 8 m (Figures 3b–3d). In order to compute 95% confidence intervals for r, we use Fisher's r-z transformation. Here r values are converted to a normally distributed z, according to $z = 0.5 \times ln[(1 + r)/(1 - r)]$, with standard error $se = 1/\sqrt{n - 3}$, where n is the number of profiles. The upper and lower limits of the confidence intervals are then computed as $[\exp(2 \times (z \pm Z_{95} \times se) - 1)]/[\exp(2 \times (z \pm Z_{95} \times se) + 1)]$, where Z_{95} is 1.96.

2.5. Model Output: B-SOSE

In section 4.2, we demonstrate the utility of long-term, multiyear biogeochemical data sets like the DPT for biogeochemical model evaluation, in particular, using seasonal nutrient variability as an important tool in diagnosing model biases in surface ocean pCO_2. The Biogeochemical Southern Ocean State Estimate (B-SOSE; Verdy & Mazloff, 2017) is a novel resource that combines observations with a general circulation ocean model to resolve and realistically represent the physical and biogeochemical state of the Southern Ocean. B-SOSE synthesizes all available Southern Ocean observing systems, assimilating in situ conductivity-temperature-depth profiles (including instrumented seals), XBT sections, Argo floats, BGC-Argo floats, satellite remote sensing, the Global Ocean Data Analysis Project (GLODAP version 2), and the Surface Ocean CO_2 Atlas (SOCAT version 4) data; see Verdy and Mazloff (2017) for assimilated data set references.

The ocean biogeochemical and physical state is simulated using the MIT general circulation model (MITgcm; Marshall et al., 1997) at 1/3° resolution poleward of 30° S, with decreasing resolution toward the equator. Vertically, B-SOSE is on a z coordinate grid with 52 vertical layers, with an approximate 4-m layer thickness in the surface ocean. The biogeochemical state is simulated using a modified Biogeochemistry with Light, Iron, Nutrient, and Gases model (BLING; Galbraith et al., 2010; Verdy & Mazloff, 2017) which includes eight prognostic tracers (alkalinity, dissolved inorganic carbon [DIC], inorganic and organic nitrogen and phosphorus, iron, and oxygen) and three phytoplankton groups (small, large, and diazotrophs). Biological activity is influenced by light, nitrate, phosphate, iron availability, and temperature and influences carbon and oxygen concentrations. Atmospheric pCO_2 is prescribed using CarbonTracker data (Peters et al., 2007), seawater pCO_2 is derived as a function of carbonate chemistry (Follows et al., 2006; Williams & Follows, 2011), and CO_2 flux across the air-sea interface is parameterized according to Wanninkhof (1992).

B-SOSE involves a 3-year spin up from climatologies and is then optimized according to the adjoint method, where the mismatch between the observed and simulated system is minimized (by minimizing the weighted least squares sum of the data-model misfits). Misfit reduction is achieved by adjusting the prescribed atmospheric state, which comes from the European Centre for Medium-Range Weather Forecasts ERA-interim

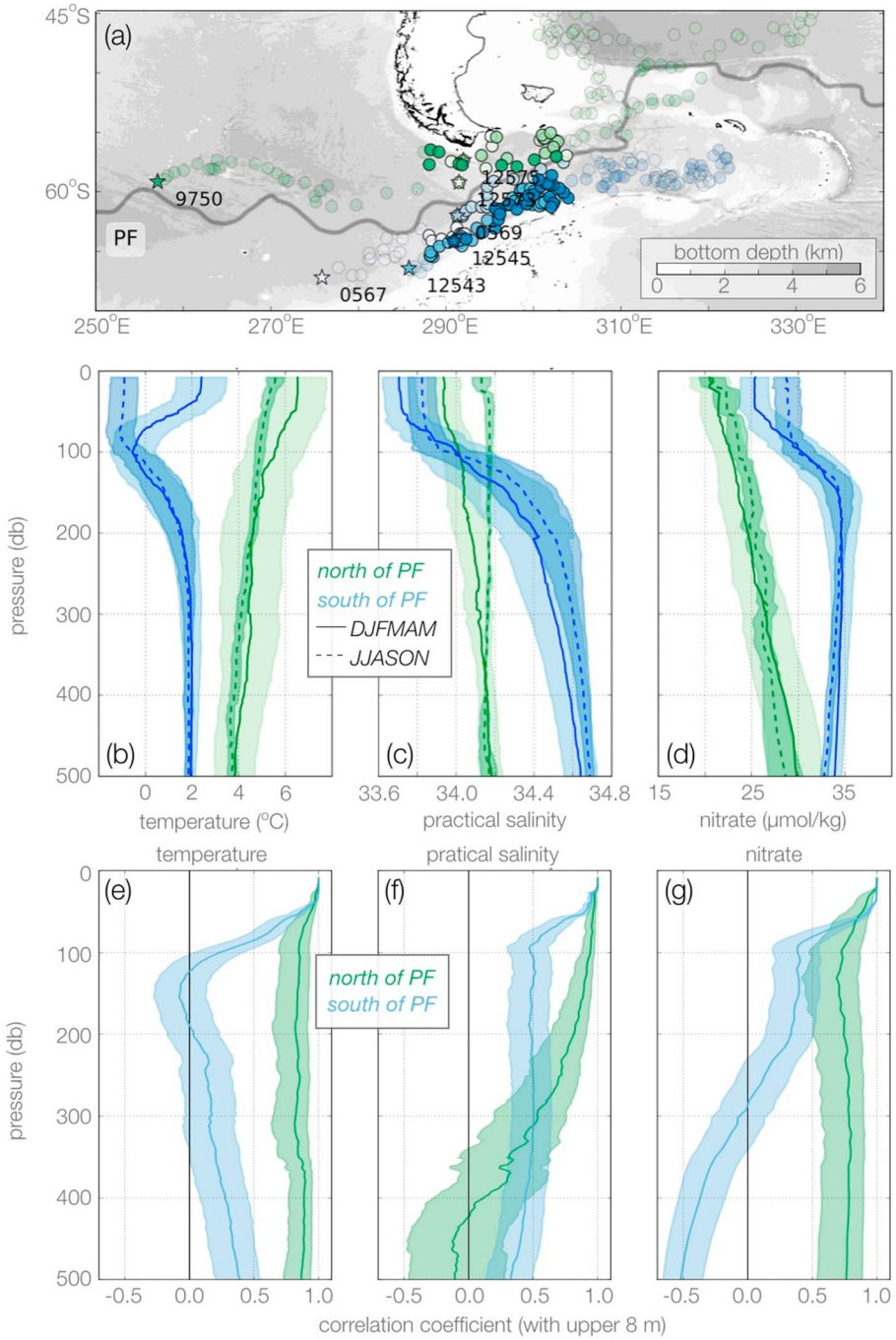

Figure 3. (a) Map of Biogeochemical-Argo float profile locations in the Drake Passage (colored circles; stars indicate deployment location; see sampling dates in Table S2). Opaque circles highlight the profiles located within the analysis domain used in (b)–(g): 288–304° E and 53–66° S. The Orsi et al. (1995) Polar Front (PF; gray contour) is overlain on ocean bottom depth (grayscale map; ETOPO1; Amante & Eakins, 2009). Floats are organized relative to the PF: three floats north of the PF (IDs 9750, 12575, and 12573; green hues) and four floats south of the PF (IDs 0567, 0569, 12545, and 12543; blue hues). Summer-autumn (DJFMAM; solid lines) and winter-spring (JJASON; dashed lines) average (b) temperature, (c) salinity, and (d) nitrate in the upper ~500 m north (green) and south (blue) of the PF; shading indicates ± one standard deviation. Correlation coefficients (r) computed for float-estimated (e) temperature, (f) salinity, and (g) nitrate concentration at depth with the surface (0–8 m) value north (green) and south (blue) of the PF (r = 1.0 indicating perfect correlation); shading indicates the 95% confidence interval.

reanalysis (Dee et al., 2011). Initial conditions are also adjusted in the optimization to better fit the data. As such, utilizing a data-assimilating model like B-SOSE has advantages over a purely forward model and can even be useful for validating the large-scale processes simulated in forward models (Russell et al., 2018). For additional information on the model configuration of the 2008–2012 solution and its extensive validation, the reader is encouraged to see Verdy and Mazloff (2017).

2.6. pCO_2 Decomposition

To diagnose any B-SOSE pCO_2 biases, we compare the seasonal cycles of underway pCO_2 (μatm), temperature, and salinity and discrete nitrate concentration from DPT observations to those estimated by B-SOSE (2008–2012; Munro, Lovenduski, Stephens, et al., 2015; Verdy & Mazloff, 2017). To avoid spatial aliasing and to match the B-SOSE time period, B-SOSE is subsampled along the main DPT line (indicated by arrows in Figure 1a) only for months when a DPT sample was collected. To highlight the observed north-south gradient across Drake Passage, we further divide this comparison into two regions, by averaging north and south of the mean XBT-defined PF along the DPT main line (58.5° S).

To parse the drivers of total pCO_2 variability on seasonal time scales, we perform a pCO_2 decomposition on DPT and B-SOSE pCO_2. We quantify the thermal ($pCO_{2(T)}$) and nonthermal ($pCO_{2(nonT)}$) components of the observed and B-SOSE total pCO_2 concentration according to the empirical equations of Takahashi et al. (2002):

$$pCO_{2(T)} : pCO_2 \; at \; T_{obs} = pCO_{2,mean} \times exp[0.0423(T_{obs} - T_{mean})], \quad (1)$$

$$pCO_{2(nonT)} : pCO_2 \; at \; T_{mean} = pCO_{2,obs} \times exp[0.0423(T_{mean} - T_{obs})], \quad (2)$$

where T is the temperature in degrees Celsisus and obs and mean subscripts denote the observed and temporal average values at each DPT/B-SOSE grid box. The thermal component approximates the pCO_2 values that would be expected from seawater temperature changes alone, whereas the nonthermal component is the proportion of pCO_2 that is driven by processes affecting the total seawater CO_2 such as biology and transport.

2.7. Additional Data Sets

We use MLD calculated from HRX XBT data (section 2.2) using a near-surface 0.2 °C threshold (Stephenson et al., 2012) to provide additional insight into the upper ocean of each frontal zone. MLD is corrected for known biases (Stephenson et al., 2012) and gridded by month and latitude to match the DPT.

Regional bathymetry, wind forcing, and freshwater forcing are important drivers of ACC dynamics. For bathymetry, we use the ETOPO1 data set, a global digital elevation model produced by the National Oceanic and Atmospheric Administration that includes ocean bathymetry and land topography data on a 1 arc min (1/60°) grid (Amante & Eakins, 2009). For wind, we use 1° merged microwave radiometer monthly wind speed (representing speeds at 10-m height) processed by Remote Sensing Systems (2016) and derived from the following satellite radiometers: Special Sensor Microwave Imager (F08 through F15), Special Sensor Microwave Imager Sounder (F16 and F17), WindSat Polarimetric Radiometer, and Advanced Microwave Scanning Radiometer (version 2; see Acknowledgments for data access and processing information). Sea ice concentration (1/4°; 2005–2017) is from Nimbus-7 Scanning Multi-channel Microwave Radiometer and DMSP Special Sensor Microwave/Imager-Special Sensor Microwave Imager/Sounder Passive Microwave Data (Cavalieri et al., 1996); sea ice extent is defined as the latitude of 15% sea ice concentration.

2.8. Statistical Analyses

We report median and percentile values to show any skewness in the DPT data within each frontal zone; percentiles (also referred to as quartiles) are calculated according to Langford (2006). Confidence intervals at the 95% level are calculated using a Z distribution for large samples sizes ($n \geq 30$; $Z = 1.96$) and a t distribution for small sample sizes ($n < 30$, with $n - 1$ degrees of freedom). Seasonal amplitude values are computed by finding the extreme values (maximum or minimum) of each season and subtracting the warm season (DJFMAM months) from the cold season (JJASON months); in some instances, where monthly data are sparse, these extreme values are determined from the maximum or minimum 3-month average (section 3.1.2).

Table 1
State[a] of Major Frontal Zones in Drake Passage (2004–2017)

	CZ	SAZ	PFZ	AAZ	SZ
			Biogeochemical		
Silicate (μmol/kg)	2.2 (1.4–3.1)	4.6 (3.0–6.5)	6.7 (4.1–9.8)	21.6 (16.0–29.6)	40.5 (27.4–52.3)
Nitrate (μmol/kg)	11.9 (8.5–14.0)	20.6 (19.0–21.4)	22.8 (21.5–24.2)	25.7 (24.7–26.8)	26.3 (23.9–27.8)
Phosphate (μmol/kg)	1.0 (0.8–1.1)	1.5 (1.4–1.5)	1.6 (1.5–1.7)	1.7 (1.7–1.8)	1.8 (1.7–2.0)
			Physical		
Temperature (°C)	7.6 (6.5–8.5)	5.6 (5.0–6.0)	4.5 (3.8–5.3)	0.7 (−0.7–1.9)	−0.5 (−1.3–1.0)
Salinity (psu)	32.9 (32.6–33.2)	34.1 (34.0–34.1)	34.0 (34.0–34.1)	33.8 (33.7–33.9)	33.9 (33.8–34.0)
MLD[b](m)	48.0 (29.4–87.5)	141.4 (87.1–225.8)	82.7 (44.6–144.4)	70.7 (48.3–99.4)	75.0 (58.3–96.4)

Note. MLD = mixed layer depth; CZ = Coastal Zone; SAZ = Subantarctic Zone; PFZ = Polar Frontal Zone; AAZ = Antarctic Zone; SZ = Southern Zone.
[a]Median value (Q1–Q3); rounded to the nearest tenth. [b]2004–2011 values (Stephenson et al., 2012).

3. Results

In this study, we aim to better understand the time-varying physical and biogeochemical fronts and zones across the ACC using macronutrient, temperature, and salinity data from the DPT. From 2004–2017, DPT silicate, nitrate, and phosphate surface concentrations range from 0.098–110.2, 0.51–33.1, and 0.23–2.3 μmol/kg, respectively. Surface temperature and salinity range from −1.8–9.6 °C and 32.09–34.18 psu, respectively. Concurrently, the monthly mean locations of the physical ACC fronts along the DPT main line span the following latitudes: the SAF between 55.2° and 57.8 °S, the PF between 56.5° and 60.0 °S, and the SACCF between 58.3° and 64.6 °S.

In section 3.1, we characterize the surface signature of the four major frontal zones, demarcated by the three XBT-defined ACC fronts. In this framework, we describe the average surface property distributions of each frontal zone and how these properties vary on seasonal time scales, driven by unique biological and physical influences locally. At the boundaries of these frontal zones are sharp gradients in nutrients important for local phytoplankton communities. In section 3.2, we find multiple surface expressions of the Nitrate Front (NF) and SF and highlight the decoupling of these two nutrients poleward of the PF. In section 3.3, we employ subsurface in situ data to gauge how representative the DPT sampling scheme is of the surface mixed layer and find it to be robust. In section 3.4, we follow our DPT results with a targeted analysis aimed at the biogeochemical modeling community, which demonstrates the utility of year-round biogeochemical time series such as the DPT in model development.

3.1. Biogeochemical Zonation of the Drake Passage

3.1.1. Background State

In general, surface macronutrients increase from north to south across Drake Passage (Table 1), consistent with previous Southern Ocean studies (e.g., Broecker & Peng, 1982; Paparazzo et al., 2016; Rubin, 2003; Williams et al., 2018). Northern Drake Passage, within the SAZ and PFZ, is relatively warm and salty with deep mixed layers. Median silicate concentration is at near-limiting levels for the local diatom population (Nelson et al., 2001), at 4.6 and 6.7 μmol/kg, respectively. Median nitrate concentration in the SAZ and PFZ is 20.6 and 22.8 μmol/kg, respectively. Median phosphate concentration in the SAZ and PFZ is 1.5 and 1.6 μmol/kg, respectively, reflecting a median N:P stoichiome\uline{}tric relationship less than the classical Redfield ratio of 16:1 (13.9:1 and 14.3:1, respectively; Figure S1; Redfield, 1934).

In contrast, surface waters in southern Drake Passage are more than 4° colder, richer in macronutrients, and characterized by shallower mixed layers. Here silicate concentrations are significantly higher than in the northern zones, with median values of 21.6 and 40.5 μmol/kg in the AAZ and SZ, respectively. Nitrate and phosphate concentrations are also higher south of the PF, with median values of 25.7 and 1.7 μmol/kg in the AAZ and 26.3 and 1.8 μmol/kg in the SZ, respectively, and retain their stoichiometric relationship slightly below Redfield (at 14.6:1 and 14.4:1, respectively; Figure S1). The silicate-to-nitrate ratio increases across the PF and SACCF, from 0.31:1 in the PFZ to 0.90:1 in the AAZ and reaching an average 1.55:1 in the SZ (Figure S1), suggesting the presence of iron-limited diatoms (Rubin, 2003; Takeda, 1998). Note that

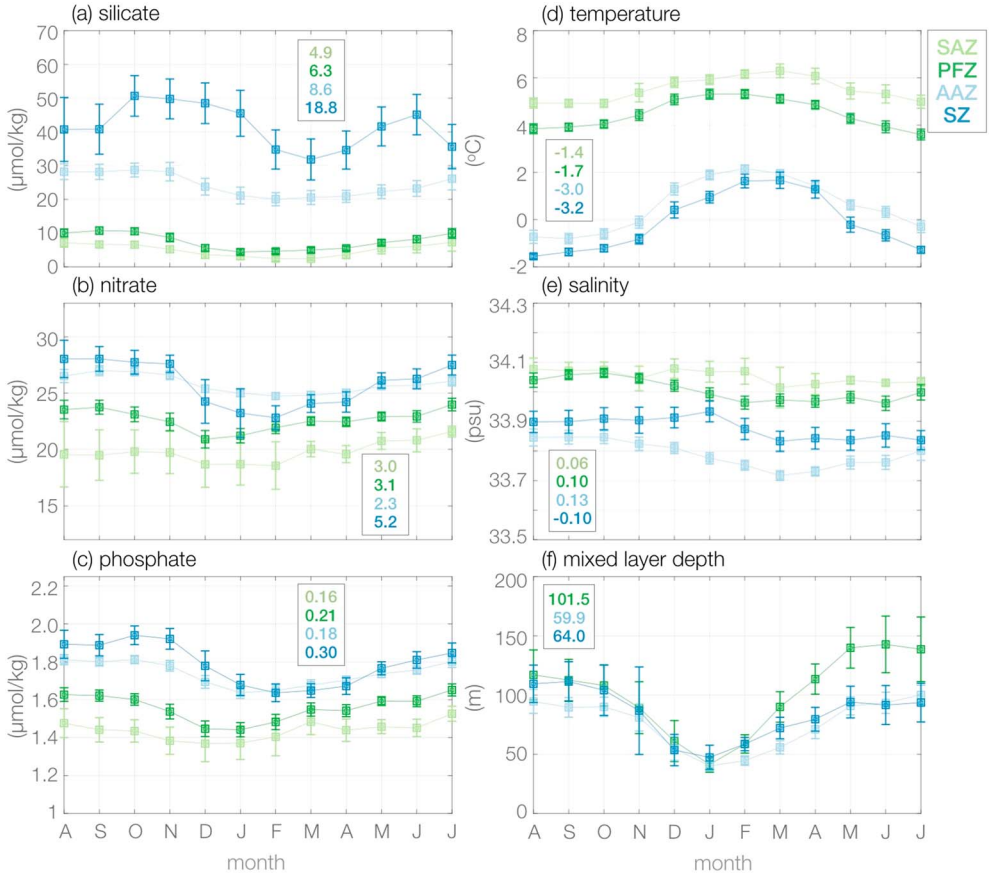

Figure 4. From 2004–2017, 3-month mean (squares; centered on month indicated) and 95% confidence interval (whiskers) of Drake Passage Time-series (a) silicate, (b) nitrate, and (c) phosphate concentration, (d) temperature and (e) salinity, and (g) mixed layer depth (2004–2011 only; Stephenson et al., 2012), colored by frontal zone: Subantarctic Zone (SAZ; light green), Polar Frontal Zone (PFZ; dark green), Antarctic Zone (AAZ; light blue), and Southern Zone (SZ; dark blue). Note that the *x* axes are ordered from August to July. Due to few observations in some months (e.g, July in the SZ), we quantify these metrics over 3-month periods and display these quantities on the center month (e.g., *D* indicates the November-December-January 3-month average). To compute the seasonal amplitude (text, colored by zone), we subtract the extreme 3-month mean value of the warm season (DJFMAM) from that of the cold season (JJASON). Seasonal cycles for the Coastal Zone are not shown and, due to large variability, SAZ mixed layer depth data are not shown in (f).

these observed nutrient ratios vary both spatially and temporally as a function of phytoplankton group and process, encompassing seasonal production, regeneration, export, and physical mixing processes.

Given the anomalously warm, fresh, and nutrient-poor surface waters observed in the first few DPT sampling locations off South America, we delineate the CZ from the open ocean frontal zones by the 2,000-m isobath. Indeed, while 2004–2017 DPT salinities range between 32.1 and 34.2 psu, the lower value is representative of the fresh waters of the CZ (median salinity value of 32.9 psu; Table 1). In this frontal zone framework, the SAZ and PFZ in the north are relatively saltier than southern Drake Passage, as low as 33.8 psu in the AAZ and as high as 34.1 psu in the SAZ (Table 1).

3.1.2. Seasonal Variability
3.1.3. Physical

The temporal and spatial variability of the locations of physical ACC fronts is evident in Figure 1a, as the XBT-defined time-varying frontal zones do not consistently fall between the Orsi et al. (1995) fronts as seen by comparing time-varying colors to static dashed front contours. Indeed, the locations of the SAF, PF, and SACCF, and the surface area of their associated frontal zones, vary month-to-month (not shown), dominated by interannual changes rather than seasonal drivers (Freeman et al., 2016; Sprintall, 2003). Between 2004 and 2017, the median location (interquartile range) of the SAF, PF, and SACCF along the DPT main line is

55.8° (55.6–56.3°) S, 58.4° (58.2–58.9°) S, and 62.1° (61.3–62.4°) S, respectively, with the SACCF exhibiting the largest N-S variability.

Despite the lack of seasonality in XBT-defined ACC front locations, we find that the physical and biogeochemical surface water mass characteristics of each time-varying frontal zone exhibit a clear and distinct seasonal cycle (Figure 4). In the Drake Passage, surface temperatures decrease poleward year-round (Figure 4d). Frontal zones are warmest in late summer-early autumn and coldest in late winter-early spring. Temperatures reach a maximum average temperature in the SAZ in March (7.0 °C observed in March 2013) and a minimum average temperature in the SZ in August (−1.8 °C observed in August 2011). Across Drake Passage, MLDs shoal in summer and deepen through winter, with a smaller seasonal amplitude observed south of the PF (Figure 4f). Here surface waters are colder (Figure 4d) and fresher (Figure 4e) year-round. The seasonal amplitudes of temperature and salinity increase poleward. For example, the seasonal temperature amplitude increases from −1.4 °C in the SAZ to −3.2 °C in the SZ (Figure 4e). This is in contrast to the circumpolar BGC-Argo study of Williams et al. (2018) that finds the seasonal amplitude of temperature to decrease poleward. Whether this is driven by methodological, sampling differences, or the uniqueness of the Drake Passage is unknown.

In southern Drake Passage, seasonal variability in salinity largely reflects local sea ice dynamics (Figure 4e; see section 4; Ducklow et al., 2013; Vernet et al., 2008). Frontal zones tend to be saltiest in winter and spring, when sea ice is present, and freshest in summer and autumn, when sea (and glacial) ice is melting. The AAZ is the freshest frontal zone year-round, while the SAZ becomes the saltiest during the warm season. Notably, the magnitude of the November-March change in salinity increases poleward, with the most pronounced freshening occurring over December-February in the SZ. The SZ is saltier than the AAZ to its north on annual (Table 1) and seasonal time scales, with largest differences in AAZ-SZ salinity in summer and autumn when temperatures are warmest and sea ice is in retreat.

3.1.4. Biogeochemical

Nutrient variability largely reflects seasonal variations in biology (photosynthesis and remineralization) and circulation (vertical mixing). Surface silicate, nitrate, and phosphate concentrations are lowest during the phytoplankton growing season (summer-autumn) due to biological utilization and highest in winter-spring, driven by a combination of upwelling and remineralization (Figures 4a–4c). While these general characteristics hold across nutrients, the seasonal cycles of these macronutrients differ in amplitude, timing, and by zone, suggesting distinct local phytoplankton dynamics and physical circulation (Rubin, 2003). We do not find seasonal nutrient variability to be dominated by variations in salinity (via dilution or concentration effects; Friis et al., 2003) and discuss other possible drivers in section 4.

As with temperature and salinity, seasonal silicate variability increases poleward, likely reflecting the presence of diatoms at these higher latitudes, with largest seasonal amplitude in the SZ (18.8 μmol/kg; Figure 4a). However, we find an apparent bimodal seasonal cycle in SZ silicate to be curious (drawdown in summer and winter; Figure 4a), suggesting a secondary removal mechanism in winter. In this instance, we speculate that this bimodal signature is likely the result of a combination of sampling bias and gridding scheme: Few winter SZ silicate observations (e.g., two total in July 2016 and 2017) combined with large SZ surface area variability suggest lower silicate concentrations more typical of the AAZ. As no other observational network is consistently sampling for silicate at these latitudes in winter, we cannot yet validate this bimodal nature until more DPT winter silicate observations are collected.

On annual time scales, we find that mean surface nitrate and phosphate concentration increases poleward (section 3.1.1 and Table 1), with the largest drawdown observed in the SZ. However, on seasonal time scales, this poleward increase does not hold for nitrate in all months (Figure 4b). Indeed, nitrate concentration in the SZ exceeds the AAZ in winter and spring, but in summer months, nitrate drawdown drives SZ concentrations significantly lower than the AAZ. This observed seasonal change in nitrate distribution south of the PF is found to be independent of seasonal changes in phosphate. We also find that the timing of maximum silicate drawdown in the SZ differs from that of nitrate, occurring later in the season (January-March compared to November-February). Given the diverse nutrient requirements across phytoplankton groups, such seasonal differences in nutrient availability likely suggest differences in local phytoplankton community composition.

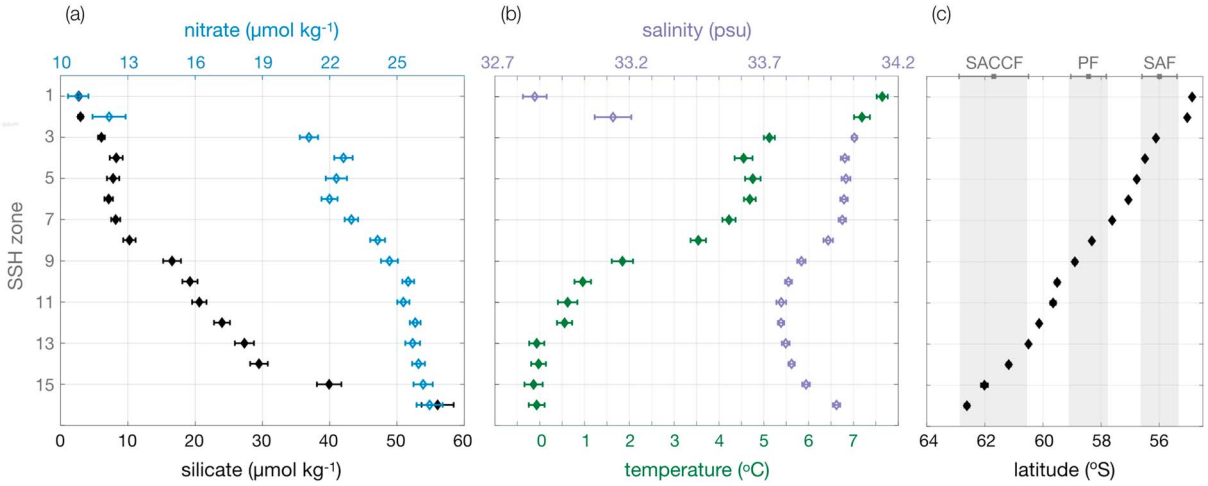

Figure 5. (colored diamonds) Mean (a) silicate (black) and nitrate (blue) concentration, (b) temperature (green), and salinity (purple) by sea surface height (SSH) zone across Drake Passage (2004–2017; whiskers denote the standard error of the mean). Here Drake Passage Time-series (DPT) data are gridded according to the SSH zone binning scheme outlined in section 2.1.1 (Figure 1b and Table S1). (c) Mean latitudes of DPT samples within each SSH zone (black diamonds); the mean latitude (gray squares; whiskers and shading are standard error) of the expendable bathythermograph-defined fronts are marked along the top *x* axis (observed along the DPT main line only; 2004–2017): from north to south, the Subantarctic Front (SAF), Polar Front (PF), and Southern Antarctic Circumpolar Current Front (SACCF). For example, SSH zone 1 is the northernmost bin, corresponding to latitudes of ~55°S, found north of the SAF, characterized by the lowest concentrations of nitrate and silicate, warmest temperatures, and freshest waters.

3.2. Biogeochemical Fronts

The mean state and seasonal variability of the four ACC frontal zones is detailed in the previous sections. We observe finer-scale spatial variability when we organize DPT observations by SSH zones (Figure 5). Average surface property distributions across Drake Passage (54–64°S) reflect the complexities of the coastal and ACC dynamics here. In particular, we find multiple surface expressions of the biologically and biogeographically relevant SF and NF, where silicate and nitrate exhibit sharp concentration gradients across physical ACC fronts (i.e., temperature-salinity fronts), respectively (Figure 5).

Indeed, we find a marked meridional gradient in silicate, nitrate, temperature, and salinity at each of the XBT-defined ACC fronts, with the magnitude of these gradients differing among properties and fronts (Figure 5). North of the SAF, the characteristics of the CZ detailed in section 3.1.1 are captured by the northernmost SSH zone (zone 1 at ~55°S; Figure 5), with its anomalously warm, fresh, and nutrient-poor signature. The latitudes of SAF variability are captured in SSH zones 3 and 4; upon crossing the SAF, mean surface temperature and salinity decrease and silicate and nitrate concentrations increase, marking the northern expression of the NF. South of the SAF (SSH zones 5–7), silicate, nitrate, temperature, and salinity remain relatively constant until upon crossing the PF (SSH zones 8–9), where property values change at an even greater magnitude than associated with the SAF. Here we find the southern expression of the NF and northern expression of the SF (nSF). While nitrate, temperature, and salinity exhibit little change between the PF and SACCF, silicate concentration continues to steadily increase. Within the latitudes of SACCF variability (SSH zones 14–16), salinity reverses its southward decline and increases toward the Antarctic continent, concurrent with the largest N-S increase in silicate concentration, marking the southern expression of the SF (sSF). Here temperatures reach below 0 °C, and nitrate concentrations slightly increase toward 30 μmol/kg. We discuss these findings in light of the historical and more recent literature in section 4.

3.3. Below the Surface: Upper-Ocean Biogeochemistry in Drake Passage

3.3.1. Upper 500 m From SR01

Repeat full-depth hydrographic sections occur on annual-decadal time scales and can provide key insights into the distribution of water mass properties and some necessary context for interpreting our characterization of the surface ocean using the DPT. SR01 was occupied by the LMG in early autumn 2006 (left panel of Figure 6) and again in early spring 2009 (right panel of Figure 6), providing a full-depth, high-resolution snapshot of silicate and nitrate concentration, temperature, and salinity (upper 500 m shown in Figure 6; see section 2.3).

In general, silicate and nitrate concentrations increase with increasing latitude and depth, reflecting upwelling of nutrient-rich CDW but with notable differences by variable and by season (Figures 6a and 6b

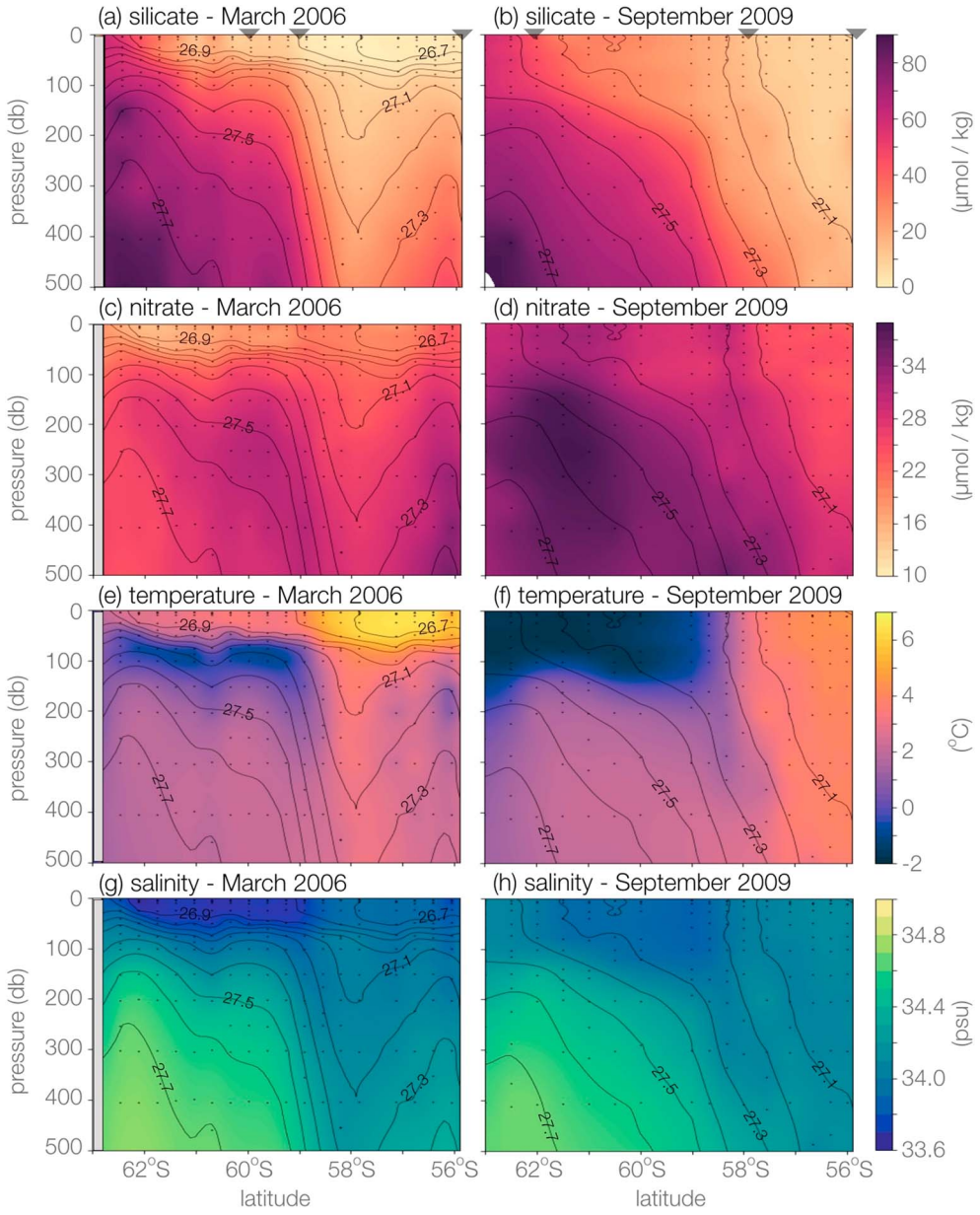

Figure 6. Silicate (a,b), nitrate (c,d), potential temperature (e,f), and salinity (g,h) distributions in the upper ~500 m collected along SR01 (section 2.3) in Drake Passage in March 2006 (left column; a, c, e, and g) and September 2009 (right column; b, d, f, and h). Black contours are lines of constant potential density anomaly (σ_Θ), and black dots are bottle locations. Along the top *x* axis, triangles indicate, from south to north, the March 2006 and September 2009 latitudinal location of the expendable bathythermograph-defined Southern Antarctic Circumpolar Current Front, Polar Front, and Subantarctic Front. Color maps follow the guidelines of Thyng et al. (2016).

and 6c and 6d, respectively). Less macronutrients remain in the upper ocean at the end of the growing season (March; left panel) relative to early spring (September; right panel). Yet more silicate remains in the upper 500 m south of the PF in March relative to nitrate (i.e., high silicate:nitrate at depth) due to the different time scales of silica dissolution and organic matter remineralization (Broecker & Peng, 1982). The surface expressions of the SF persist down to at least 500 m depth throughout the year, with the strongest lateral and vertical silicate gradients observed in summer months. Indeed, surface heating and ice-free conditions in summer create warm, stratified surface waters south of the PF (Figures 6e and 6g), conditions favorable for diatom growth and productivity. Thus, the seasonal changes in nutrient cycling driven by local phytoplankton communities and circulation result in distinct physical and biogeochemical zones in the upper 500 m of the Drake Passage.

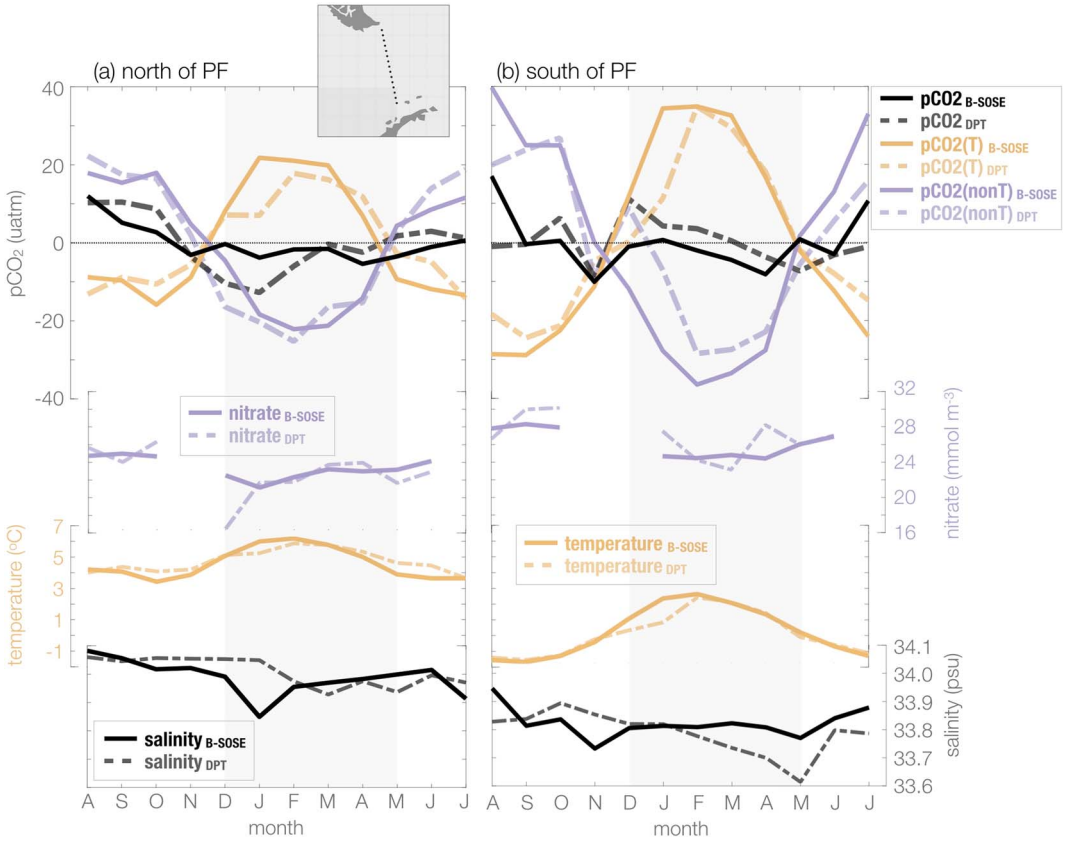

Figure 7. North (a) and south (b) of the observed mean location of the expendable bathythermograph-defined Polar Front (PF; 58.5° S), comparison of 2008–2012 monthly pCO_2 concentration anomaly (annual mean removed), nitrate, temperature, and salinity from Biogeochemical Southern Ocean State Estimate (B-SOSE) output (bold/solid; Verdy & Mazloff, 2017) and Drake Passage Time-series (DPT) observations (light/dashed); data gaps in nitrate stem from a lack of DPT nitrate observations in some months during 2008–2012. Total pCO_2 concentration (bold/soft black; top panel) is decomposed into its thermal ($pCO_{2(T)}$; bold/soft gold) and nonthermal ($pCO_{2(nonT)}$; bold/soft purple) components according to equations (1) and (2) (Takahashi et al., 2002). Note that the *x* axes are ordered from August to July; gray vertical shading denotes warm season (DJFMAM) months. B-SOSE is subsampled according to the DPT sampling scheme along the most repeated line (map inset; section 2.6).

3.3.2. Representativeness of the DPT: Mixed Layer Properties From BGC-Argo Floats

How representative is the DPT of the surface mixed layer? Using temperature, salinity, and nitrate concentration measured by BGC-Argo floats, we quantify the average property distribution and vertical structure of the upper 500 m north and south of the PF in the Drake Passage (Table S2 and Figure 3). For a given variable, regional mean differences are stark, further highlighting distinct physical and biogeochemical regimes north and south of the PF (green and blue profiles, respectively; Figures 3e–3g). South of the PF, nitrate and salinity have the same structure down to at least 100 m, with nitrate concentration increasing with increasing salinity (increasing depth). North of the PF, nitrate and temperature have opposite vertical gradients down to at least 500 m, with nitrate concentration increasing with decreasing temperature (increasing depth). Across the Drake Passage, mean BGC-Argo MLD (± one standard deviation) increases from 50.7 ± 31.5 north of the PF to 62.7 ± 24.3 south of the PF. Note that this meridional MLD gradient contradicts the XBT-based gradient presented in Figures 4f and 8 and Table 1. We largely attribute these differences to a warm season bias in the northern float profiles, due to a lack of wintertime profiles north of the PF (Table S2). Therefore, the mean BGC-Argo MLD observed in northern Drake Passage is most representative of a summertime MLD scenario and thus biased shallow.

Seasonal mean differences in nitrate, temperature, and salinity are most pronounced in the upper 100 m south of the PF: Relative to the cold season (JJASON), the warm season (DJFMAM) is characterized by a warmer, fresher, and lower nutrient surface layer (Figures 3e–3g). Indeed, 100 m marks the depth of Antarctic Surface Water (also known as Winter Water), manifested as a sharp temperature minimum layer

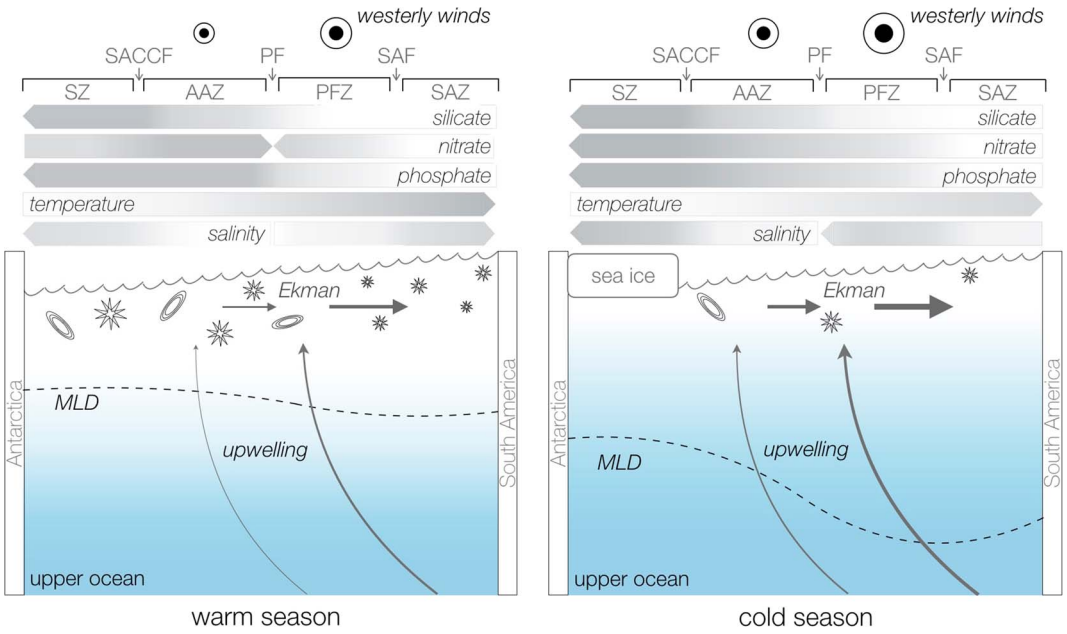

Figure 8. Schematic representation of the key physical and biogeochemical processes that set the seasonal variability of the upper ocean of Drake Passage: westerly winds (filled circle inside open circle; Remote Sensing Systems, 2016), historically defined physical Antarctic Circumpolar Current fronts and frontal zones, surface property distributions and gradients (horizontal gray gradient bars, pointing/darkening in the direction of increasing value), sea surface height (scalloped line; Archiving, Validation and Interpretation of Satellite Oceanographic), light availability (vertical blue gradient; darker at depth), small (stars; e.g., coccolithophores) and large (oval discs; e.g., diatoms) phytoplankton, wind-induced Ekman transport (horizontal, northward arrows; Munro, Lovenduski, Takahashi, et al., 2015), upwelling (vertical, surface-ward arrows; Munro, Lovenduski, Takahashi, et al., 2015), and mixed layer depth (MLD; dashed line; Stephenson et al., 2012). For illustrative purposes, size and weight of shapes and arrows are used to indicate the *relative* differences in scalar properties between the warm season (DJFMAM; left) and the cold season (JJASON; right; e.g., larger, darker, or thicker illustrations imply a greater magnitude or strength). Fronts, zones, and mixed layer are labeled as Subantarctic Front (SAF), Polar Front (PF), Southern Antarctic Circumpolar Current Front (SACCF), Subantarctic Zone (SAZ), Polar Frontal Zone (PFZ), Antarctic Zone (AAZ), Southern Zone (SZ), and MLD.

in summer, acting to decouple surface temperature from the Upper CDW temperature below. This vertical temperature inversion is also visible in Figure 6e.

We find that the discrete surface sampling scheme of the DPT robustly captures mixed layer properties. The correlation of the upper 500 m of the water column with the surface (defined as the average of the upper 8 m) varies by depth, property, region, and season (Figures 3b–3d). For our purposes, we deem a correlation strong when the confidence interval exceeds $|r| > 0.5$. North of the PF, temperature and nitrate values remain strongly correlated with the surface down to at least 500 m, while the strong correlation in salinity only persists down to ~200 m. In contrast, south of the PF, temperature, salinity, and nitrate values are only strongly correlated within the mixed layer (<100 m) but decouple below the mixed layer. These results highlight the known stratification of the region, as the PF marks the transition from a more temperature-dominated northern regime to a more salinity-dominated southern regime (Pollard et al., 2002).

3.4. Observed Versus Modeled pCO_2 and Its Drivers

Through a targeted analysis, we compare DPT observations to model output to demonstrate how observing and resolving the seasonality of nutrients can better position the biogeochemical modeling community for resolving seasonal surface ocean pCO_2 variability in models. In this targeted analysis, we employ B-SOSE output and apply the same pCO_2 decomposition method to this output and the DPT observations (equations (1) and (2); section 2.6).

Observed surface ocean pCO_2 reaches a maximum in winter and minimum in summer (top panels of Figures 7a and 7b; Munro, Lovenduski, Stephens, et al., 2015; Takahashi et al., 2002). This typical Southern Ocean pCO_2 seasonal cycle is the net result of two opposing drivers. In summer, surface heating drives an increase in surface ocean pCO_2 through an increase in $pCO_{2(T)}$. In opposition, enhanced biological produc-

tivity and the associated DIC drawdown drives a reduction in pCO_2 through $pCO_{2(nonT)}$. In winter, increased $pCO_{2(nonT)}$ is driven by vigorous wintertime mixing acting to increase DIC in the surface, while surface cooling drives an opposing $pCO_{2(T)}$.

Overall, B-SOSE performs well, with notable seasonal biases. North of the PF (Figure 7a), B-SOSE underestimates both $pCO_{2(T)}$ and $pCO_{2(nonT)}$ in summer (DJF), when drawdown is too weak and heating is too strong, translating to a high seasonal bias in total pCO_2. South of the PF (Figure 7b), B-SOSE overestimates total pCO_2 in winter (JJA), driven by a high bias in $pCO_{2(nonT)}$ and marked by a premature peak in August.

Representing the thermal and nonthermal components, B-SOSE captures the dynamic range and seasonal structure of temperature and nitrate across Drake Passage, respectively, with notable differences in salinity in the south. Comparing the seasonality of these variables provides insight into the possible sources of bias in pCO_2 and its components. We demonstrate the utility of the DPT in exploring these biases in section 4.

4. Discussion

The length (>13 years) and frequency of sampling (5–8 times per year) of the DPT is unmatched by other Southern Ocean observing networks (Figure 2 and section 4.1.2), representing the largest repository of repeat wintertime biogeochemical observations in the ACC, particularly concurrent silicate, nitrate, and phosphate observations. While the DPT has been extensively utilized for Southern Ocean carbon flux studies in recent years (e.g., Fay et al., 2018; Landschützer et al., 2015; Munro, Lovenduski, Stephens, et al., 2015; Munro, Lovenduski, Takahashi, et al., 2015), this is the first study to use the DPT to fully characterize macronutrients, particularly silicate and nitrate, on seasonal time scales and in the context of the physical and biogeochemical fronts of the ACC. We also demonstrate the value and utility of DPT nutrients to inform and improve the representation of the physical and biological processes driving Southern Ocean carbon variability in biogeochemical models (sections 3.4 and 4.2).

The biogeochemical zones of the Southern Ocean have long been understood to be home to relatively uniform property distributions (Deacon, 1982; Pollard et al., 2002), but this study highlights the smaller spatiotemporal scale variations observed across frontal zones, particularly the differences in silicate and nitrate availability and variability south of the PF. In the following sections, we present our conceptual understanding of the physical and biogeochemical processes that determine the main seasonal patterns observed in the upper ocean in Drake Passage using a schematic (section 4.1.1). We further detail the relationship between silicate and nitrate, specifically, including a discussion on the decoupling of silicate and nitrate in the context of biogeography and current observing systems (sections 4.1.1 and 4.1.2). Finally, we highlight the overall value and utility of the DPT in the observational and modeling communities (sections 4.1.2 and 4.2).

4.1. Nutrient Distributions and Biogeochemical Fronts: Biological Versus Physical Drivers of Variability

The Southern Ocean is an important site for deep water mass ventilation and transformation. The strong westerly winds over ACC latitudes drive a surface divergence (i.e., the lower and upper overturning cells; Marshall & Speer, 2012) via Ekman transport and subsequent upwelling. South of the PF, this upwelled CDW is rich in macronutrients, particularly silicate, and old (i.e., natural) carbon, signatures of its long journey from the other major ocean basins. This unique overturning circulation in the presence of biology sets up the many physical and biogeochemical fronts of the ACC and the region's biogeography.

The Southern Ocean is considered a High-Nutrient Low-Chlorophyll region, largely due to a persistent lack of iron and seasonal light limitation that weakens the efficiency of the biological pump (Boyd et al., 2000). Despite this High-Nutrient Low-Chlorophyll status, the seasonal drawdown of nutrients across Drake Passage suggests the presence of significant biological productivity (Figure 4). Indeed, from north to south, the distribution of phytoplankton communities varies according to local bottom-up (the physical-biogeochemical environment) and top-down controls (zooplankton grazing), where a mix of smaller phytoplankton (e.g., calcifying coccolithophores) tends to flourish in the north and larger phytoplankton (e.g., silicifying diatoms) dominate in the south (Balch et al., 2016; Landry et al., 2002; Rubin, 2003; Trull et al., 2018; Wright et al., 2010). This biogeography is largely determined by the availability of nutrients (including iron) across frontal zones. The silicate-rich waters of the AAZ and SZ south of the PF support a thriving diatom community (Figure 4; Petrou et al., 2016, and references therein; Balch et al., 2016; Nissen et al., 2018; Trull et al., 2018). The seasonally silicate-limited waters observed north of the PF struggle to

support high diatom productivity, but the availability of nitrate and phosphate is sufficient to support the smaller phytoplankton communities that do not require silicate (Figures 4a and 4b). Light availability may also play a role in determining biogeography across the ACC fronts since MLDs are significantly greater to the north (particularly in the SAZ) than to the south (Table 1). Understanding controls on phytoplankton composition is of critical importance since diatoms and coccolithophores are ubiquitous in this region and play significant roles in marine carbon cycling, with the ability to alter surface ocean pCO_2 through photosynthesis or calcification, recycle organic matter, and export carbon out of the surface through the ballasting effects of their shells. For the purposes of this study, we focus on these two key groups to facilitate a broad discussion of large-scale biogeography.

4.1.1. Summary of Observed Seasonal Patterns

During the warm season (DJFMAM; left panel of Figure 8), surface heating and the melting of land and sea ice stratifies the water column (MLD shoals), stimulating phytoplankton growth and productivity in the sunlit surface layer. South of the PF, macronutrients are plentiful and phytoplankton utilize available nitrate and phosphate for photosynthesis and diatoms additionally use silicate for building their hard silica shells. Under optimal conditions, diatoms take up silicate and nitrate at a 1:1 ratio (Ragueneau et al., 2000; Smetacek, 1999), but Southern Ocean diatoms are not often under optimal conditions. Largely limited by iron south of the PF and colimited by iron and silicate north of the PF (Nelson et al., 2001; Cortese & Gersonde, 2008; Hoffmann et al., 2008), diatom silicate:nitrate depletion ratios are often more than three times larger (Rubin, 2003; Takeda, 1998). The strength of the westerly winds is larger north of the PF relative to the south, which drives a similar gradient in curl-driven upwelling and Ekman transport across the Drake Passage (Munro, Lovenduski, Stephens, et al., 2015; Remote Sensing Systems, 2016). As recently upwelled waters travel northward as part of the upper cell, silicate is preferentially drawn down over nitrate (and P) by iron-stressed diatoms, effectively serving as the biophysical mechanism that sets up the SF at the PF and therefore the low-Si and high-N signature of the PFZ and SAZ (Table 1 and Figures 5 and 8; Franck et al., 2000; Leynaert et al., 2004; Takeda, 1998). The observed steepening of the sillicate-to-nitrate ratio from north to south (Figure S1) is determined by the balance of these biological and physical processes including utilization ratios, the abundance of diatoms, remineralization, and lateral and vertical transport.

Sea ice forms in the cold season (JJASON; right panel of Figure 8), with a maximum sea ice extent reaching latitudes as far north as the mean SACCF (purple contour in Figure 1a), rejecting brine and driving vertical exchange. Relatively stronger westerlies, Ekman transport, and upwelling drive strong surface cooling and enhanced mixing (Remote Sensing Systems, 2016). Deeper mixed layers allow for more surface entrainment of nutrients from below but at a time when sunlight is much reduced and biological productivity is low. The degree to which physical processes in winter (i.e., vertical mixing and northward sea ice transport) determine subsequent biological productivity in spring and summer is difficult to determine in this analysis.

4.1.2. Decoupling of Silicate and Nitrate and Implications for Observing Systems

The annual distribution and seasonal variation in silicate is clearly decoupled from that of nitrate south of the PF (Table 1 and Figures 4, 5, and S1). This is an important distinction in terms of Southern Ocean biogeography as well as having important implications for how we currently observe the Southern Ocean and interpret existing data. This study finds two surface expressions of the SF, with sharp gradients in silicate concentration at both the PF and SACCF (nSF and sSF, respectively; Figure 8), with the nSF is roughly coincident with the NF and may be the most important expression in terms of biogeography. As this is the first study to define the sSF, future studies should investigate its biogeochemical significance, particularly the degree to which these biogeochemical fronts are related to gradients in species composition/utilization ratios versus physical processes. The results of this study suggest that macronutrient observations of nitrate alone preclude the parsing of biological activity by key phytoplankton groups, and without concurrent nitrate and silicate observations, we miss a great deal of information that describes the biological processes from the dominant Southern Ocean phytoplankton group, the silicifiers. For example, a nitrate sensor is included in the suite of biogeochemical sensors deployed on BGC-Argo floats, but the technology for a float-based silicate sensor does not yet exist. While data from these floats have dramatically increased the number of intraseasonal biogeochemical observations in the last few years, the lack of concurrent silicate observations precludes the analysis of the influence of phytoplankton biogeography on carbonate chemistry variability. The DPT is the only multiyear, intraseasonal time series of coordinated sampling across the ACC, particularly of silicate and nitrate, that no other Southern Ocean observing platform currently provides. As a climate record that includes winter months, the DPT can provide important validation of autonomous systems (e.g., nitrate sensors on BGC-Argo floats and gliders).

4.2. Utility of the DPT as a Model Metric

The majority of models have pCO_2 biases, and reducing these biases is an active area of research (see Jiang et al., 2014; Mongwe et al., 2018). Recent studies demonstrate that models that accurately reproduce pCO_2 on seasonal time scales are more skillful at capturing pCO_2 variability on longer time scales and are therefore important for climate change simulations (Gregor et al., 2018; Gruber et al., 2019). In order to diagnose these model biases, validation studies have focused on examining the modeled versus observed pCO_2 decomposition, comparing the seasonal cycles of total pCO_2, $pCO_{2(T)}$, and $pCO_{2(nonT)}$ (demonstrated in section 3.4). In doing so, the goal is to determine whether pCO_2 biases are largely driven by biases in modeled temperature and/or biology and mixing. Indeed, $pCO_{2(T)}$ reflects cooling in winter and warming in summer, resulting in a winter-to-summer increase in pCO_2. In contrast, $pCO_{2(nonT)}$ variability is dominated by seasonal variations in DIC. Wintertime mixing and biological respiration increase DIC, and net biological uptake draws it back down in summer, resulting in a winter-to-summer decrease in pCO_2.

Seeking a more complete picture of the processes driving biases in B-SOSE pCO_2 and its thermal and nonthermal components, we compare the seasonal cycles of nitrate, temperature, and salinity as a first-order validation (Figure 7 and section 3.4). The data assimilating nature of B-SOSE provides a more realistic representation of the physical and biogeochemical state of the Southern Ocean to within model error. First-order validation of $pCO_{2(T)}$ and $pCO_{2(nonT)}$ lies in B-SOSE's ability to resolve the seasonal cycles of temperature and nitrate, respectively. In this targeted analysis, we find that B-SOSE is generally in good agreement with the DPT, capturing the observed seasonality in nitrate, temperature, and $pCO_{2(T)}$, even resolving the observed north-south gradient in nitrate concentration, a bias typically found in some forward models (Freeman et al., 2018). These results suggest that pCO_2 drivers other than temperature and those associated with nitrate cycling in the model are biased. While dilution does not appear to affect nitrate, the wintertime salinity bias south of the PF is suspect. We speculate that too much sea ice formation in B-SOSE, and therefore too much brine rejection, drives a high salinity bias south of the PF in winter, likely influencing DIC and driving the wintertime $pCO_{2(nonT)}$ bias. Indeed, Rosso et al. (2017) show the large effect of DIC dilution from sea ice melt and precipitation at these southerly latitudes.

How does DIC vary seasonally in B-SOSE? What mechanisms could drive differences in DIC:nitrate? Future work on fully diagnosing these biases and improving B-SOSE's representation of pCO_2 can now begin with investigating DIC. Quantifying the seasonal cycles of nitrate, temperature, and salinity in addition to performing a pCO_2 decomposition allowed us to make more inferences about the drivers of B-SOSE pCO_2 biases than a decomposition alone. Future work should also involve implementing silicate as an active tracer in future B-SOSE estimates. Given that this study finds the distribution and variability of silicate and nitrate to be notably different, particularly south of the PF, we could argue that nitrate variability provides an incomplete picture of the biological drivers that might impact $pCO_{2(nonT)}$. Indeed, whether the addition of silicate as a prognostic variable in B-SOSE would provide more insight into the effects of different biological communities on pCO_2 in Drake Passage is an open question (e.g., the ratio of coccolithophores and diatoms).

5. Conclusions

We quantify the mean state and seasonal variability of biogeochemical properties and associated fronts in the Drake Passage (2004–2017) using the longest year-round biogeochemical ship-based data set in the Southern Ocean. Using BGC-Argo floats in Drake Passage, we confirm the DPT's robust representation of the mixed layer. South of the PF, silicate and nitrate are decoupled on seasonal to annual time scales, driven by a combination of physical and biological processes, including the likely presence of iron-stressed diatoms. We find two surface expressions of the SF, the nSF and sSF, associated with the latitudes of PF and SACCF variability, respectively, with the nSF being the most important in terms of the biogeography of the region. As this is the first study to define the sSF, future studies should investigate its biogeochemical significance, such as its role in enhancing or inhibiting the cross-frontal exchange of silicate at these latitudes.

Through a targeted analysis, we demonstrate the utility of the DPT in enhancing current biogeochemical model evaluation techniques. We compare the observed DPT seasonal cycles of surface-ocean pCO_2, its thermal and nonthermal components, temperature, salinity, and nitrate concentration to those estimated by B-SOSE in Drake Passage. While B-SOSE skillfully resolves nitrate variations on seasonal time scales, biases still persist in the nonthermal pCO_2 component, and therefore total pCO_2, most notably south of the PF in winter months. These results suggest biases in B-SOSE DIC:nitrate, likely tied in part to a high wintertime salinity bias driving dilution effects, and lay the groundwork for model improvements. To first order, a

Acknowledgments
We thank the ARSV *Laurence M. Gould* marine and science support teams for their collection of DPT discrete and underway samples (available at www.ldeo.columbia.edu/res/pi/CO2/carbondioxide/pages/global_ph.html); nutrient analyses were performed at Chesapeake Biological Laboratory and the Oceanographic Data Facility at Scripps Institution of Oceanography. XBT data are made freely available by the Scripps High Resolution XBT program (www-hrx.ucsd.edu/ax22.html). Cruise reports for SR01 data (Sweeney et al., 2012) and SOCCOM deployment cruises can be found on the CLIVAR and Carbon Hydrographic Data Office (CCHDO) website (https://cchdo.ucsd.edu/); in using CCHDO, we acknowledge the NSF/NOAA-funded U.S. Repeat Hydrography Program. BGC-Argo data were collected and made freely available by the Southern Ocean Carbon and Climate Observations and Modeling (SOCCOM) Project funded by the National Science Foundation, Division of Polar Programs (NSF PLR-1425989), supplemented by NASA, and by the International Argo Program and the NOAA programs that contribute to it (www.argo.ucsd.edu.argo.jcommops.org). The Argo Program is part of the Global Ocean Observing System. The SOCCOM data used here are available online (doi.org/10.6075/J0QJ7FJP; *Snapshot 2018-09-12*; Johnson et al., 2018). B-SOSE is an integral part of the SOCCOM project and output can be found on the SOSE website (www.sose.ucsd.edu). AVISO SSH products are provided by the Copernicus Marine and Environment Monitoring Service (CMEMS). Microwave radiometer wind speed data are processed by Remote Sensing Systems with funding from the NASA Earth Science MEaSUREs Program and the NASA Earth Science Physical Oceanography Program (accessible at www.remss.com). This work has benefited from discussions with Ariane Verdy. We thank Gordon R. Stephenson Jr. for providing the XBT-derived MLD values from his 2012 study and Lynne Talley for providing objective mapping code for gridding the SR01 data.
N. M. F. is grateful for support from the John B. McKee Foundation for educational and general purposes for Scripps Institution of Oceanography and the G. Unger Vetlesen Foundation to support Scripps' global change research effort. D. R. M. and C. S. were supported by NSF award 1543457. J. S. was supported by NSF Award 1542902. M. R. M. and I. R. were supported by NSF's Southern Ocean Carbon and Climate Observations and Modeling (SOCCOM) Project under the NSF Award PLR-1425989, with additional support from NOAA and NASA;

model that does not skillfully simulate observed seasonal nutrient cycling cannot hope to skillfully and accurately simulate the observed seasonal pCO_2 cycle; otherwise, that model is merely getting the right answer for the wrong reason. As the biogeochemical modeling community continues to work toward constraining estimates of the strength of the Southern Ocean carbon sink, the seasonal nutrient cycles presented here can serve as a benchmark.

References

Amante, C., & Eakins, B. W. (2009). ETOPO1 1 Arc-Minute Global Relief Model: Procedures, data sources and analysis (*NGDC-24*): National Geophysical Data Center, NOAA.

Baker, D. J., Nowlin, W. D., Pillsbury, R. D., & Bryden, H. L. (1977). Antarctic Circumpolar Current: Space and time fluctuations in the Drake Passage. *Nature*, *268*, 696–699. https://doi.org/10.1038/268696a0

Balch, W. M., Bates, N. R., Lam, P. J., Twining, B. S., Rosengard, S. Z., Bowler, B. C., et al. (2016). Factors regulating the Great Calcite Belt in the Southern Ocean and its biogeochemical significance. *Global Biogeochemical Cycles*, *30*, 1124–1144. https://doi.org/10.1002/2016GB005414

Boyd, P. W., Watson, A. J., Law, C. S., Abraham, E. R., Trull, T., Murdoch, R., et al. (2000). A mesoscale phytoplankton bloom in the polar Southern Ocean stimulated by iron fertilization. *Nature*, *407*(6805), 695–702. https://doi.org/10.1038/35037500

Broecker, W. S., & Peng, T.-H. (1982). Tracers in the sea. A publication of the Lamont-Doherty Geological Observatory.

Bryden, H. (1973). New polynomials for thermal expansion, adiabatic temperature gradient and potential temperature of seawater. *Deep-Sea Research*, *20*, 401–408. https://doi.org/10.1016/0011-7471(73)90063-6

Cavalieri, D. J., Parkinson, C. L., Gloersen, P., & Zwally, H. (1996). Sea ice concentrations from Nimbus-7 SSMR and DMSP SSM/I-SSMIS passive microwave data, updated yearly.

Cortese, G., & Gersonde, R. (2008). Plio/Pleistocene changes in the main biogenic silica carrier in the Southern Ocean, Atlantic Sector. *Marine Geology*, *252*, 100–110.

de Boyer Montégut, C., Madec, G., Fischer, A. S., Lazar, A., & Iudicone, D. (2004). Mixed layer depth over the global ocean: An examination of profile data and a profile-based climatology. *Journal of Geophysical Research*, *109*, C12003. https://doi.org/10.1029/2004JC002378

Deacon, G. E. R. (1933). A general account of the hydrology of the South Atlantic Ocean. Discovery Rep., VII, 177-238.

Deacon, G. E. R. (1937). The hydrology of the Southern Ocean. Discovery Rep., XV, 1-124.

Deacon, G. E. R. (1982). Physical and biological zonation in the Southern Ocean. *Deep-Sea Research*, *29*(1), 1–15.

Dee, D. P., Uppala, S. M., Simmons, A. J., Berrisford, P., Poli, P., Kobayashi, S., et al. (2011). The ERA-Interim reanalysis: Configuration and performance of the data assimilation system. *Quarterly Journal of the Royal Meteorological Society*, *137*, 553–597.

Donohue, K. A., Tracey, K. L., Watts, D. R., Chidichimo, M. P., & Chereskin, T. K. (2016). Mean Antarctic Circumpolar Current transport measured in Drake Passage. *Geophysical Research Letters*, *43*, 760–767. https://doi.org/10.1002/2016GL070319

Ducklow, H. W., Fraser, W. R., Meredith, M. P., Stammerjohn, S. E., Doney, S. C., Martinson, D. G., et al. (2013). West Antarctic Peninsula: An ice-dependent coastal marine ecosystem in transition. *Oceanography*, *26*(3), 190–203. https://doi.org/10.5670/oceanog.2013.62

Fay, A. R., Lovenduski, N. S., McKinley, G. A., Munro, D. R., Sweeney, C., Gray, A. R., et al. (2018). Utilizing the Drake Passage TIme-series to understand variability and change in subpolar Southern Ocean pCO_2. *Biogeosciences*, *15*, 3841–3855.

Fofonoff, P., & Millard, R. C. Jr. (1983). Algorithms for computation of fundamental properties of seawater. UNESCO Technical Papers in Marine Sciences, 44, 55 pp.

Follows, M. J., Ito, T., & Dutkiewicz, S. (2006). On the solution of the carbonate chemistry system in ocean biogeochemistry models. *Ocean Modell*, *12*(3–4), 290–301. https://doi.org/10.1016/j.ocemod.2005.05.004

Franck, V. M., Brzezinski, M. A., Coale, K. H., & Nelson, D. M (2000). Iron and silicic acid concentrations regulate Si uptake north and south of the Polar Frontal Zone in the Pacific Sector of the Southern Ocean. *Deep-Sea Research II*, *47*, 3315–3338.

Freeman, N. M., Lovenduski, N. S., & Gent, P. R. (2016). Temporal variability in the Antarctic Polar Front (2002–2014). *Journal of Geophysical Research: Oceans*, *121*, 7263–7276. https://doi.org/10.1002/2016JC012145

Freeman, N. M., Lovenduski, N. S., Munro, D. R., Krumhardt, K. M., Lindsay, K., Long, M. C., & Maclennan, M. (2018). The variable and changing Southern Ocean Silicate Front: Insights fromt he CESM Large Ensemble. *Global Biogeochemical Cycles*, *32*, 752–768. https://doi.org/10.1029/2017GB005816

Friis, K., Körtzinger, A., & Wallace, D. W. R. (2003). The salinity normalization of marine inorganic carbon chemistry data. *Geophysical Research Letters*, *30*(2), 1085. https://doi.org/10.1029/2002GL015898

Frölicher, T. L., Sarmiento, J. L., Paynter, D. J., Krasting, J. P., & Winton, M. (2014). Dominance of the Southern Ocean in anthropogenic carbon and heat uptake in CMIP5 models. *Journal of Climate*, *28*, 862–886.

Galbraith, E. D., Gnanadesikan, A., Dunne, J. P., & Hiscock, M. R. (2010). Regional impacts of iron-light colimitation in a global biogeochemical model. *Biogeosciences*, *7*, 1043–1064.

Gille, S. T. (2014). Meridional displacement of the Antarctic Circumpolar Current. *Philosophical Transactions of the Royal Society A: Mathematical, Physical and Engineering Sciences*, *372*, 20130273.

Graham, R. M., De Boer, A. M., Heywood, K. J., Chapman, M. R., & Stevens, D. P. (2012). Southern Ocean fronts: Controlled by wind or topography? *Journal of Geophysical Research*, *117*, C08018. https://doi.org/10.1029/2012JC007887

Gregor, L., Kok, S., & Monteiro, P. M. S. (2018). Interannual drivers of the seasonal cycle of CO_2. *Biogeosciences*, *15*, 2361–3278.

Gruber, N., Landschützer, P., & Lovenduski, N. S. (2019). The variable Southern Ocean carbon sink. *Annual Review of Marine Science*, *11*, 159–186.

Hanawa, K., Rual, P., Bailey, R., Sy, A., & Szabados, M. (1995). A new depth-time equation for Sippican or TSK T-7, T-6 and T-4 expendable bathythermographs (XBT). *Deep-Sea Research I*, *42*, 1423–1451.

Hoffmann, L. J., Peeken, I., & Lochte, K. (2008). Iron, silicate, and light co-limitation of three Southern Ocean diatom species. *Polar Biology*, *31*, 1067–1080.

Jiang, C. L., Gille, S. T., Sprintall, J., & Sweeney, C. (2014). Drake Passage oceanic pCO_2: Evaluating CMIP5 coupled carbon-climate models using in situ observations. *Journal of Climate*, *27*, 76–100.

Johnson, K. S., Riser, S. C., Boss, E. S., Talley, L. D., Sarmiento, J. L., Swift, D. D., et al. (2018). SOCCOM float data—Snapshot 2018-09-12. In Southern Ocean Carbon and Climate Observations and Modeling (SOCCOM) Float Data Archive. UC San Diego Library Digital Collections, https://doi.org/10.6075/J0QJ7FJP

Joyce, T. M., Zenk, W., & Toole, J. M. (1978). The anatomy of the Antarctic polar front in the Drake Passage. *Journal of Geophysical Research*, *83*(C12), 6093–6113.

logistical support for SOCCOM was provided by NSF through the U.S. Antarctic Program. S. G. P. was supported by U.S. GO-SHIP through NSF grant OCE-1437015. C. A. D. was supported by a NSF GEO/OCE REU site grant (NSF award 1659793) to Scripps Institution of Oceanography.

Landry, M. R., Selph, K. E., Brown, S. L., Abbott, M. R., Measures, C. I., Vink, S., et al. (2002). Seasonal dynamics of phytoplankton in the Antarctic Polar Front region at 170° W. *Deep-Sea Res II*, *49*, 1843–1865.

Landschützer, P., Gruber, N., Haumann, F. A., Rodenbeck, C., Bakker, D. C. E., van Heuven, S., et al. (2015). The reinvigoration of the Southern Ocean carbon sink. *Science*, *349*(1221).

Langford, E. (2006). Quartiles in elementary statistics. *Journal of Statistics Education*, *14*(3), 1–20. https://doi.org/10.1080/10691898.2006.11910589

Lenn, Y.-D., Chereskin, T. K., Sprintall, J., & Firing, E. (2007). Mean jets, mesoscale variability and eddy momentum fluxes in the surface layer of the Antarctic Circumpolar Current in Drake Passage. *Journal of Marine Research*, *65*, 27–58.

Lenton, A., Tilbrook, B., Law, R., Bakker, D., Doney, S. C., Gruber, N., et al. (2013). Sea-air CO_2 fluxes in the Southern Ocean for the period 1990–2009. *Biogeosciences Discussions*, *10*, 285–333.

Leynaert, A., Bucciarelli, E., Claquin, P., Dugdale, R. C., Martin-Jézéquel, V., Pondaven, P., & Ragueneau, O. (2004). Effect of iron deficiency on diatom cell size and silicic acid uptake kinetics. *Limnology and Oceanography*, *49*(4I), 1134–1143.

Marshall, J., Adcroft, A., Hill, C., Perelman, L., & Heisey, C. (1997). A finite-volume, incompressible Navier Stokes model for studies of the ocean on parallel computers. *Journal of Geophysical Research*, *102*(C3), 5753–5766.

Marshall, J., & Speer, K. (2012). Closure of the meridional overturning circulation through Southern Ocean upwelling. *Nature Geoscience*, *5*, 171–180. https://doi.org/10.1038/NGEO1391

Matsumoto, K., Sarmiento, J. L., & Brzezinski, M. A. (2002). Silicic acid leakage from the Southern Ocean: A possible explanation for glacial atmospheric pCO_2. *Global Biogeochemical Cycles*, *16*(3), 1031. https://doi.org/10.1029/2001GB001442

Mongwe, N. P., Chang, N., & Monteiro, P. M. S. (2016). The seasonal cycle as a mode to diagnose biases in modelled CO_2 fluxes in the Southern Ocean. *Ocean Modelling*, *106*, 90–103.

Mongwe, N. P., Vichi, M., & Monteiro, P. M. S. (2018). The seasonal cycle of pCO_2 and CO_2 fluxes in the Southern Ocean: Dignosing anomalies in CMIP5 Earth system models. *Biogeosciences*, *155*, 2851–2872.

Moore, J. K., Fu, W., Primeau, F., Britten, G. L., Lindsay, K., Long, M., et al. (2018). Sustained climate warming drives declining marine biological productivity. *Science*, *359*, 1139–1143.

Munro, D. R., Lovenduski, N. S., Stephens, B. B., Newberger, T., Arrigo, K. R., Takahashi, T., et al. (2015). Estimates of net community production in the Southern Ocean determined from time series observations (2002–2011) of nutrients, dissolved inorganic carbon, and surface ocean pCO_2 in Drake Passage. *Deep-Sea Res II*, *114*, 49–63.

Munro, D. R., Lovenduski, N. S., Takahashi, T., Stephens, B. B., Newberger, T., & Sweeney, C. (2015). Recent evidence for a strengthening CO_2 sink in the Southern Ocean from carbonate system measurements in the Drake Passage (2002–2015). *Geophysical Research Letters*, *42*, 7623–7630. https://doi.org/10.1002/2015GL065194

Nelson, D. M., Brzezinski, M. A., Sigmon, D. E., & Franck, V. M. (2001). A seasonal progression of Si limitation in the Pacific sector of the Southern Ocean. *Deep Sea Research Part II: Topical Studies in Oceanography*, *48*(19–20), 3973–3995.

Nissen, C., Vogt, M., Münnich, M., Gruber, N., & Haumann, F. A. (2018). Factors controlling coccolithophore biogeography in the Southern Ocean. *Biogeosciences*, *15*, 6997–7024.

Orsi, A. H., Whitworth, W., & Nowlin, W. D. (1995). On the meridional extent and fronts of the Antarctic Circumpolar Current. *Deep Sea Research Part I: Oceanographic Research Papers*, *42*(5), 641–673.

Palter, J. B., Marinov, I., Sarmiento, J. L., & Gruber, N. (2013). Large-scale, persistent nutrient fronts of the World Ocean: Impacts on biogeochemistry. In I. M. Belkin (Ed.), *Chemical oceanography of frontal zones*. Berlin Heidelberg: Springer-Verlag.

Paparazzo, F. E., Alder, V. A., Schloss, I., Bianchi, A., & Esteves, J. L. (2016). Spatial and temporal trends in the distribution of macronutrients in surface waters of the Drake Passage. *Ecologia Austral*, *26*, 27–39.

Peters, W., Jacobson, A. R., Sweeney, C., Andrews, A. E., Conway, T. J., Masarie, K., et al. (2007). An atmospheric perspective on North American carbon dioxide exchange: CarbonTracker. *Proceedings of the National Academy of Sciences of the United States of America*, *104*(48), 18925–18930.

Petrou, K., Kranz, S. A., Trimborn, S., Hassler, C. S., Blanco Ameijeiras, S., Sackett, O., et al. (2016). Southern Ocean phytoplankton physiology in a changing climate. *Journal of Plant Physiology*, *203*, 135–150.

Pollard, R. T., Lucas, M. I., & Read, J. F. (2002). Physical controls on biogeochemical zonation in the Southern Ocean. *Deep Sea Research Part II*, *49*, 3289–3305.

Ragueneau, O., Tréguer, P., Leynaert, A., Anderson, R. F., Brzezinski, M. A., DeMaster, D. J., et al. (2000). A review of the Si cycle in the modern ocean: Recent progress and missing gaps in the application of biogenic opal as a paleoproductivity proxy. *Global and Planetary Change*, *26*(4), 317–365.

Redfield, A. C. (1934). *On the proportions of organic derivatives in sea water and their relation to the composition of plankton*, pp. 177–192. Liverpool: Liverpool University Press. vol. James Johnstone Memorial Volume.

Remote Sensing Systems (2016). [updated Nov 2018], Monthly mean wind speed data set on a 1 degree grid made from Remote Sensing Systems Version-7 Microwave Radiometer Data, V0701, [accessed on 8 Jan 2018]. Santa Rosa, CA, USA, Santa Rosa, CA, USA, Available at www.remss.com.

Rintoul, S. R. (2018). The global influence of localized dynamics in the Southern Ocean. *Nature*, *558*, 209–218.

Rintoul, S. R., Hughes, C., & Olbers, D. (2001). The Antarctic Circumpolar Current System. In G. Siedler, J. Church, & J. Gould (Eds.), *Ocean circulation and climate* pp. 271–302). San Diego; Sydney: Academic Press.

Rödenbeck, C., Bakker, D. C. E., Gruber, N., Iida, Y., Jacobson, A. R., Jones, S., et al. (2015). Data-based estimates of the ocean carbon sink variability—First results of the Surface Ocean pCO_2 Mapping intercomparison (SOCOM). *Biogeosciences*, *12*, 7251–7278.

Rosso, I., Mazloff, M. R., Verdy, A., & Talley, L. D. (2017). Space and time variability of the Southern Ocean carbon budget. *Journal of Geophysical Research: Oceans*, *122*, 7407–7432. https://doi.org/10.1002/2016JC012646

Rubin, S. I. (2003). Carbon and nutrient cycling in the upper water column across the Polar Frontal Zone and Antarctic Circumpolar Current along 170W. *Global Biogeochemical Cycles*, *17*(3), 1087. https://doi.org/10.1029/2002GB001900

Russell, J. L., Kamenkovich, I., Bitz, C., Ferrari, R., Gille, S. T., Goodman, P. J., et al. (2018). Metrics for the evaluation of the Southern Ocean in Coupled Climate Models and Earth System Models. *Journal of Geophysical Research: Oceans*, *123*, 3120–3143. https://doi.org/10.1002/2017JC013461

Sallée, J. B., Speer, K., & Morrow, R. (2008). Response of the Antarctic Circumpolar Current to Atmospheric Variability. *Journal of Climate*, *21*(12), 3020–3039.

Sarmiento, J. L., Gruber, N., Brzezinski, M. A., & Dunne, J. P. (2004). High-latitude controls of thermocline nutrients and low latitude biological productivity. *Nature*, *427*, 56–60.

Sievers, H. A., & Emery, W. J. (1978). Variability of the Antarctic polar frontal zone in the Drake Passage - summer 1976–1977. *Journal of Geophysical Research*, *83*(C6), 3010–3022.

Smetacek, V. (1999). Diatoms and the ocean carbon cycle. *Protist*, *150*, 25–32.
Sokolov, S., & Rintoul, S. R. (2009). Circumpolar structure and distribution of the Antarctic Circumpolar Current fronts: 1. Mean circumpolar paths. *Journal of Geophysical Research*, *114*, C11018. https://doi.org/10.1029/2008JC005108
Sprintall, J. (2003). Seasonal to interannual upper-ocean variability in the Drake Passage. *Journal of Marine Research*, *61*, 27–57.
Stephenson, G. R. Jr, Gille, S. T., & Sprintall, J. (2012). Seasonal variability of upper ocean heat content in Drake Passage. *Journal of Geophysical Research*, *117*, C04019. https://doi.org/10.1029/2011JC007772
Swart, N. C., Gille, S. T., Fyfe, J. C., & Gillett, N. P. (2018). Recent Southern Ocean warming and freshening driven by greenhouse gas emissions and ozone depletion. *Nature Geoscience*, *11*, 836–841.
Sweeney, C., Newberger, T., & Guilderson, T. (2012). Carbon dioxide, hydrographic, and chemical data obtained during the R/V Laurence M. Gould cruise in the Southern Ocean on CLIVAR Repeat Hydrography Sections A21 (March 21–April 4, 2006). Oak Ridge, Tennessee: Carbon Dioxide Information Analysis Center, Oak Ridge National Laboratory, US Department of Energy.
Takahashi, T., Olafsson, J., Goddard, J. G., Chipman, D. W., & Sutherland, S. C. (1993). Seasonal variation of CO_2 and nutrients in the high-latitude surface oceans: A comparitive study. *Global Biogeochemical Cycles*, *7*, 843–878.
Takahashi, T., Sutherland, S. C., Sweeney, C., Poisson, A., Metzl, N., Tilbrook, B., et al. (2002). Global sea-air CO_2 flux based on climatolgoical surface ocean pCO_2, and seasonal biological and temperature effects. *Deep-Sea Research II*, *49*, 1601–1622.
Takeda, S. (1998). Influence of iron availability on nutrient consumption ratio of diatoms in oceanic waters. *Nature*, *393*, 774–777.
Thyng, K. M., Greene, C. A., Hetland, R. D., Zimmerle, H. M., & DiMarco, S. F. (2016). True colors of oceanography: Guidelines for effective and accurate colormap selection. *Oceanography*, *29*(3), 9–13.
Toggweiler, J. R., & Samuels, B. (1995). Effect of Drake Passage on the global thermohaline circulation. *Deep-Sea Research I*, *42*(4), 477–500.
Trull, T. W., Passmore, A., Davies, D. M., Smit, T., Berry, K., & Tilbrook, B. (2018). Distribution of planktonic biogenic carbonate organisms in the Southern Ocean south of Australia: A baseline for ocean acidification impact assessment. *Biogeosciences*, *15*, 31–49.
Verdy, A., & Mazloff, M. R. (2017). A data assimilating model for estimating Southern Ocean biogeochemistry. *Journal of Geophysical Research: Oceans*, *122*, 6968–6988. https://doi.org/10.1002/2016JC012650
Vernet, M., Martinson, D., Iannuzzi, R., Stammerjohn, S. E., Kozlowski, W., Sines, K., et al. (2008). Primary production within the sea-ice zone west of the Antarctic Peninsula: I—Sea ice, summer mixed layer, and irradiance. *Deep Sea Research Part II*, *55*, 2068–2085. https://doi.org/10.1016/j.dsr2.2008.05.021
Wanninkhof, R. (1992). Relationship between wind speed and gas exchange. *Journal of Geophysical Research*, *97*(C5), 7373–7382.
Williams, N. L., Juranek, L. W., Feely, R. A., Russell, J. L., Johnson, K. S., & Hales, B. (2018). Assessment of the carbonate chemistry seasonal cycles in the Southern Ocean from persistent observational platforms. *Journal of Geophysical Research: Oceans*, *123*, 4833–4852. https://doi.org/10.1029/2017JC012917
Williams, R. G., & Follows, M. J. (2011). *Ocean Dynamics and the Carbon Cycle: Principles and Mechanisms*. Cambridge, UK: Cambridge University Press.
Winter, J. B. L., Henderiks, A., Rickaby, R. E. M., & Brown, C. W. (2013). Poleward expansion of the coccolithophore Emiliania huxleyi. *Journal of Plankton Research*, *36*, 316–325.
Wright, S. W., van den Enden, R. L., Pearce, I., Davidson, A. T., Scott, F. J., & Westwood, K. J. (2010). Phytoplankton community structure and stocks in the Southern Ocean (30–80E) determined by CHEMTAX analysis of HPLC pigment signatures. *Deep-Sea Research Part II*, *57*, 758–778.